

The memory of Rayleigh-Taylor turbulence

Sébastien Thévenin^{1,2}, Benoît-Joseph Gréa^{1,2}, Gilles Kluth^{1,2} and Balu Nadiga³

¹ CEA, DAM, DIF, F-91297 ArpaJon, France

² Université Paris-Saclay, CEA, Laboratoire Matière en Condition Extrême, 91680 Bruyères-le-Châtel, France

³ Los Alamos National Laboratory, Los Alamos, NM, USA

(Received ?; revised ?; accepted ?. - To be entered by editorial office)

We examine the issue of the memory of initial conditions in the various stages of a canonical flow driven by Rayleigh-Taylor instabilities. We do this by developing and using a set of tools based on data-driven machine learning techniques and Bayesian inference. The data consist of a set of direct numerical simulations (DNS) conducted within the framework of small-density contrast miscible fluids, where the initial interface deformation, constituting the initial conditions (IC), is determined by an annular spectrum parametrized by four non-dimensional numbers. The region of IC parameters considered spans the regimes of inertial and diffusive growth of the mixing layer. We seek to infer the IC parameters associated with the mixing zone given instantaneous measurements of a set of domain-averaged, zero-dimensional (0D) turbulent quantities at an unspecified time, while noting complications arising from the presence of qualitatively different— inertial and diffusive—regimes. We achieve this by first building a forward surrogate for the 0D turbulent quantities of interest using a physics-constrained neural network and demonstrating its ability to extrapolate into parameter regions not accessible to DNS. Then, within a Bayesian framework that uses the surrogate, we employ a Markov-Chain Monte-Carlo method to infer the posterior distribution of ICs given instantaneous measurements of the set of 0D turbulent quantities. This approach helps us characterize and shed new light on how ICs are progressively forgotten during the transition to turbulence. Furthermore, this method allows us to select sets of turbulent quantities that best preserve the memory of the ICs and thus are best suited to predict the future evolution of Rayleigh-Taylor mixing zones. This main line of Bayesian inference is complemented by a global sensitivity analysis we conduct to disentangle the effects of the IC parameters on the growth of the mixing layer. The results and insights obtained from Bayesian inference are then tied back to the results of the sensitivity analysis. Finally, we propose a strategy to model the Rayleigh-Taylor transition to turbulence that iteratively infers the posterior distribution of ICs and forward propagates its maximum a posteriori (MAP).

Key words: Rayleigh-Taylor instability, turbulent mixing, Physics-informed Machine learning, Bayesian inference

1. Introduction

Turbulent mixing in multi-component materials is a fundamental process observed in astrophysical (Porth *et al.* 2014; Hillier 2018), geophysical flows (Fernando 1991; Gregg *et al.* 2018) and also in engineering applications such as inertial confinement fusion (ICF) (Lindl 1995; Nakai & Takabe 1996; Hurricane *et al.* 2024; Abu-Shawareb *et al.* 2024).

Controlling the perturbations at the fuel/ablator interface of an ICF capsule is crucial to reduce the mixing, which has depleting effects on the ignition. In fluids or plasma, turbulent mixing often occurs where density gradients are present along with strong accelerations denoted by g . This configuration is at the origin of many phenomena such as gravity waves, the Richtmyer-Meshkov instability (Thornber *et al.* 2010) and the Faraday instability (Briard *et al.* 2020; Cavelier *et al.* 2022). Complex acceleration histories have been shown to have an important impact on the mixing layer dynamics (Dimonte *et al.* 2007; Ramaprabhu *et al.* 2013; Livescu *et al.* 2021; Aslangil *et al.* 2022; Morgan 2022). The Rayleigh-Taylor instability (RTI) (Rayleigh 1882; Taylor 1950) is particularly important among buoyancy-driven flows due to its ability to efficiently convert potential energy into mixing (Davies Wykes & Dalziel 2014).

The RTI thus occurs when a light fluid pushes a heavy one or equivalently when a heavy fluid is placed on top of a lighter one in a gravity field (Boffetta & Mazzino 2017; Zhou 2017; Zhou *et al.* 2021). Classical RTI dynamics involve the growth of a mixing zone from an initially perturbed interface, successively punctuated by different regimes (Sharp 1984). In the context of miscible fluids, the early linear phase (Chandrasekhar 1961; Duff *et al.* 1962) occurs immediately, or after a diffusive process, depending on the characteristic length of the main interface defects. When all initial modes are stable, with their wavelengths being smaller than the cut-off scale determined by the dispersion relationship, unstable larger wavelength can still be produced by a slow backscatter process. The mixing zone later enters a potential non-linear regime where the dominant spikes or bubbles evolve toward a constant terminal velocity (Layzer 1955; Cook & Dimotakis 2001; Goncharov 2002; Ramaprabhu *et al.* 2006; Bian *et al.* 2020; Gréa & Briard 2023). Secondary shear instabilities, produced between the rising and falling structures, trigger the transition to turbulence, leading to the formation of a turbulent mixing zone (Cook *et al.* 2004). When the density contrast, expressed by the Atwood number (\mathcal{A}), is small, variable density effects manifest primarily through the buoyancy force, and the layer keeps a top/bottom statistical symmetry (Ramaprabhu & Andrews 2004; Livescu 2013). At late time, the dimensional analysis suggests the existence of a final regime where the mixing zone width, L , grows as $2\alpha Agt^2$ with t the time and α classically denoting the self-similar growth rate (Dalziel *et al.* 1999; Ristorcelli & Clark 2004; Mueschke *et al.* 2006; Vladimirova & Chertkov 2009; Morgan *et al.* 2017).

Whether the growth parameter is universal or not has been an ongoing debate in the past decades. A wide range of α values, from 0.02 to 0.1, have been reported in both experiments or simulations, which, for a modelling perspective, has significant implications (Young *et al.* 2001; Dimonte *et al.* 2004; Ramaprabhu *et al.* 2005). Beyond the difficulty of reaching the RTI's final regime, particularly due the confinement of the growing large-scale structures, the most resolved simulations (Cook & Cabot 2006; Livescu 2013; Morgan & Black 2020; Briard *et al.* 2022) or well controlled experiments (Roberts & Jacobs 2016) agree on the lower values $\alpha \sim 0.02 - 0.03$. Furthermore, the perturbations at the initial interface seem to have an impact (Youngs 2013). Depending on whether the initial modes are at large or small scales, it has been observed that the final value of α either slightly evolves or remains constant (Dimonte 2004). This phenomenon has been linked to mode competition or mode coupling. Therefore, it appears that the RTI, even in its final self-similar turbulent regime, retains the memory of its initial conditions.

Besides, it comes as no surprise that the mixing layer growth is also related to the large scales of the flow. From the rapid acceleration model, a formula for α has been derived, showing its dependence on global mixing and the dimensionality parameter that expresses the elongation of large scale structures along the vertical direction (Gréa 2013). The imprint of the coherent structures on the dynamics of RTI has also been

evidenced through the analysis of the infrared slope of turbulent spectra (Poujade & Peybernes 2010; Soulard *et al.* 2015). However, except for homogeneous configurations that satisfy the generalized principle of permanence of large eddies, these studies cannot explicitly demonstrate the relationship between the final regime and the initial conditions of buoyancy-driven flows such as RTI.

More recently, Kord & Capecelatro (2019) demonstrate the ability of adjoint-based methods to evaluate the sensitivity of the Rayleigh-Taylor mixing to its initial conditions. The study also successfully derives the optimal interface perturbations to dampen or enhance the RTI growth in its late stages. Beyond the challenges of applying an adjoint method when the initial perturbation involves a very large number of modes, this study clearly suggests that the distribution of the initial perturbation is crucial when modelling the RTI.

Therefore, the objective of this work is to use a statistical Bayesian approach to model the RTI process, taking into account the distribution of initial perturbations. The approach aims to infer the initial conditions of RTI from the model's state variables, and then leverage this information to predict the evolution of turbulent quantities. This procedure closely examines the extent to which the RTI retains or forgets its initial conditions.

This work is organized as follows: We first present the RTI database obtained from DNS and the surrogate model developed to reproduce the 0D turbulent quantities. Then, we perform a sensitivity analysis to identify the influence of each initial parameter across the different RTI regimes. In the final section, we detail the methodology for inferring the initial conditions of RTI from 0D observations and the modelling of the RTI transition to turbulence based on the maximum a posteriori initial conditions.

2. Direct numerical simulations and surrogate model

2.1. Basic equations and RTI initial setup

The binary mixture produced by the RTI can be characterized by the velocity vector $\mathbf{u}(\mathbf{x}, t) = (u_x, u_y, u_z)^T$ and the concentration of heavy fluid $C(\mathbf{x}, t)$ with $\mathbf{x} = (x, y, z)^T$ defining the position in a Cartesian frame and t denoting the time. In the limit of small Atwood number ($\mathcal{A} \rightarrow 0$) and neglecting compressibility effects, this system is typically described by the Navier-Stokes equations under the Boussinesq approximation

$$\nabla \cdot \mathbf{u} = 0, \quad (2.1a)$$

$$\partial_t \mathbf{u} + \mathbf{u} \cdot \nabla \mathbf{u} = -\nabla \Pi - 2\mathcal{A}gC \mathbf{e}_z + \nu \nabla^2 \mathbf{u}, \quad (2.1b)$$

$$\partial_t C + \mathbf{u} \cdot \nabla C = \kappa \nabla^2 C. \quad (2.1c)$$

The equation (2.1a) stands as the incompressibility condition, while in the momentum equation, Eq. (2.1b), Π is the reduced pressure and ν the kinematic viscosity. For this configuration, the acceleration ($g > 0$), appearing in the buoyancy term, is oriented downward along the z vertical direction indicated by the unit basis vector \mathbf{e}_z . In the transport equation for the concentration C , Eq. (2.1c), the diffusion coefficient κ is here fixed such that the Schmidt number is unity ($Sc = \nu/\kappa = 1$).

At the initial time ($t = 0$), we assume the fluid is at rest ($\mathbf{u} = 0$), and a heavy fluid (concentration $C = 1$) is located above a lighter fluid (concentration $C = 0$) separated by a diffuse interface at $z = 0$ and of width δ . The initial concentration field C is thus defined by

$$C(\mathbf{x}, t = 0) = \frac{1}{2} (1 + \tanh [3(z - \eta(x, y))/\delta]), \quad (2.2)$$

with $\eta(x, y)$ being a zero mean 2π -periodic initial perturbation at the interface. This per-

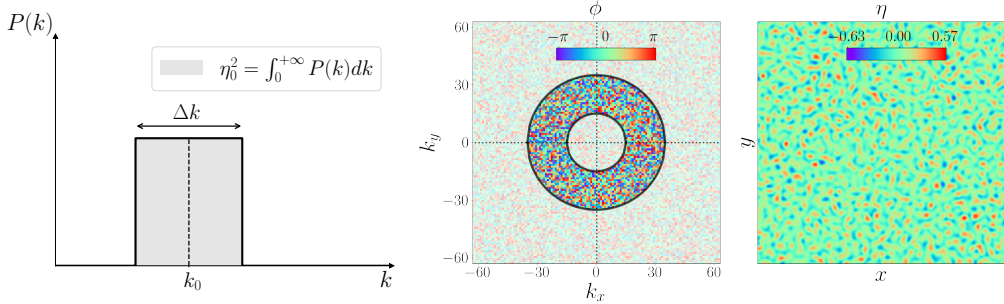


Figure 1: Initial perturbation of the interface with: (Left) the Fourier power spectrum of the perturbation amplitude, (Middle) the phase of the Fourier modes (middle) and (Right) the perturbation amplitude in the physical space.

turbation is further characterized by the horizontal discrete Fourier modes $\hat{\eta}$ of wavevector $\mathbf{k} = (k_x, k_y)^T \in \mathbb{Z}^2$ and modulus $k = \|\mathbf{k}\|$ such that

$$\eta(x, y) = \sum_{\mathbf{k} \in \mathbb{Z}^2} \hat{\eta}(\mathbf{k}) e^{i(k_x x + k_y y)}. \quad (2.3)$$

The realizability condition, $\eta \in \mathbb{R}$, imposes that for the complex Fourier modes $\hat{\eta}(-\mathbf{k}) = \hat{\eta}^*(\mathbf{k})$. In this work, we further consider an annular spectrum for the interface perturbation, Eq. (2.3), as in Dimonte *et al.* (2004) of the form

$$\hat{\eta}(\mathbf{k}) = e^{i\phi(\mathbf{k})} \times \begin{cases} cst/k & \text{for } \|k - k_0\| \leq \Delta k/2 \\ 0 & \text{for } \|k - k_0\| > \Delta k/2 \end{cases} \quad \text{with } \eta_0 = \int_0^{+\infty} P(k) dk = \left(\int \hat{\eta} \hat{\eta}^* d^2 \mathbf{k} \right)^{1/2}. \quad (2.4)$$

Here in Eq. (2.4), k_0 is the mean wavenumber, η_0 is the *rms* amplitude, Δk is the bandwidth of the perturbation, ϕ the phase of modes and $P(k)$ the perturbation spectrum of the interface. The figure 1 provides an illustration of the initial perturbation in which each phase ϕ is randomly sampled.

Therefore, given the phase ϕ and the wavenumber k_0 , the initial conditions are fully determined by four nondimensional numbers, namely

$$\mathbf{R} = \frac{\sqrt{\mathcal{A}gk_0}}{\nu k_0^2}, \quad \mathbf{B} = \frac{\Delta k}{k_0}, \quad \mathbf{S} = k_0 \eta_0, \quad \text{and } \mathbf{D} = k_0 \delta. \quad (2.5)$$

In equation (2.5), \mathbf{R} stands as an initial perturbation Reynolds number based on the classical linear growth rate $\sqrt{\mathcal{A}gk_0}$ and expressing the balance between the inertial and the dissipative effects. In addition, \mathbf{B} indicates a narrow or large band multi-mode perturbation. The renormalized diffusion thickness is provided by \mathbf{D} and \mathbf{S} measures the steepness of the interface perturbation.

2.2. A large database of RTI simulations

To explore the impact of initial conditions on the RTI, we solve the Navier-Stokes equations under the Boussinesq approximation, Eqs. (2.1a)-(2.1c), using our pseudo-spectral code *Stratospec* (Viciconte *et al.* 2019; Gréa & Briard 2019; Briard *et al.* 2020, 2022). Our study encompasses a series of 3D simulations within a triply periodic domain sized $(2\pi)^2 \times (4\pi)$, elongated in the vertical direction z . These simulations are conducted on a $1024^2 \times 2048$ grid, starting from a state where the flow velocity is at rest, and the initial perturbed interface is aligned with the set-up described earlier in Sec. 2.1.

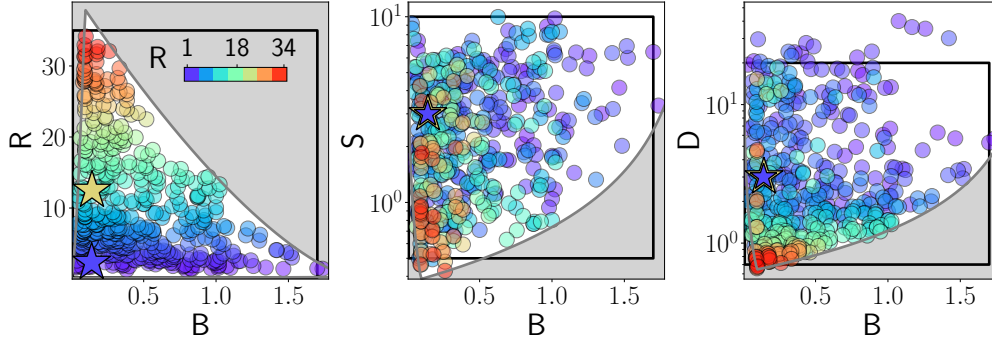


Figure 2: Distribution of the DNS in the four-dimensional initial conditions space $\{R, B, S, D\}$. Every marker corresponds to a simulation and it is coloured according to its rank in the value of R (red corresponds to a high value and purple to a low one). The grey areas correspond to infeasible DNS due to constraints and precautions taken to ensure a good numerical resolution. The blue and yellow star symbols indicate the parameters for the diffusive and inertial simulations detailed in section 2.3. The rectangles delimit the domain where the global sensitivity analysis is performed.

We have compiled a substantial database of direct numerical simulations (DNS) by varying the quartet of the initial conditions, denoted as $\mathbf{l} = (R, B, S, D)^T$, while maintaining a consistent random seed for the phase ϕ . Throughout these simulations, the Atwood number, the Schmidt number and the viscosity are held constant at $\mathcal{A} = 0.05$, $Sc = 1$ and $\nu = 7.5 \times 10^{-4}$ (in arbitrary unit), respectively. The chosen viscosity ensures that, for a gravity $g \leq 150$, the smallest turbulent scales are well-resolved, with the ratio between the Kolmogorov scale ℓ_K and the grid spacing $\Delta x = (2\pi)/1024$ consistently exceeding $\frac{1}{2}$. The maximum initial non zero wavenumber in these simulations is $k = 341$.

To mitigate the effects of scale confinement, which could adversely affect the dynamics of the mixing layer at later stages, we exclude wavenumbers below 20 that have non-zero amplitude in the initial spectral band. This restriction, alongside ensuring that the initial interface thickness (δ) and the perturbation amplitude (η_0) are sufficiently resolved ($\delta \geq 5\Delta x$ and $\eta_0 \geq 3\Delta x$, respectively), outlines the numerical constraints challenging the simultaneous achievement of a high Reynolds number (R) and a broad initial mode bandwidth (B). The distribution of our DNS across the space of initial parameters is illustrated in the figure 2, highlighting areas where simulations become numerically infeasible due to these constraints. In total, the database comprises 467 DNS, executed on massively parallel architectures at an approximate computational cost of 30 million CPU hours.

Using the linear stability analysis of a diffuse interface driven by the RTI, it is possible to express γ_0^* , the non-dimensionalized exponential growth rate corresponding to the mean wavenumber k_0 as a function of the parameters R and D

$$\gamma_0^*(R, D) = \frac{\nu^{1/3}}{(\mathcal{A}g)^{2/3}} \gamma_0 = \frac{1}{R^{4/3}} \left(\left(\frac{R^2}{\psi(D)} + 1 \right)^{1/2} - 2 \right) \text{ with } \psi(D) = 1 + \frac{2\sqrt{2}}{3} D. \quad (2.6)$$

This formula (2.6) is obtained using the results of Duff *et al.* (1962) in the low Atwood number limit and taking $1/\|dC/dz\|_{\max} = 2\delta/3$ for the diffusion thickness. Also from the equation (2.6), one recovers the inertial limit for $R \gg 1$ and $D \ll 1$ leading to the classical inviscid growth rate, $\gamma_0 = \sqrt{\mathcal{A}gk_0}$. By contrast, the RTI is stabilized in the

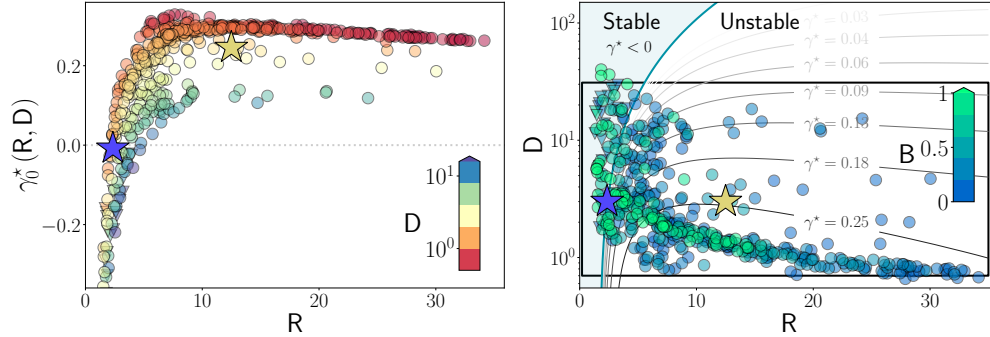


Figure 3: (Left) Linear growth rate γ_0^* and (Right) stability diagram of the mean wavenumber k_0 for all simulations. Circular markers (\circ) correspond to simulations in which there is at least one unstable wavenumber whereas downward triangles (∇) correspond to simulations where all wavenumbers in the initial spectral band are stable. The symbol color is related to the diffusive thickness D (Left), or to the parameter B (Right) expressing if the simulation is narrow or large bandwidth. The two blue and yellow \star symbols indicate the parameters for the diffusive and inertial simulations discussed in the section 2.3. The rectangles define the hyper-cubic domain \mathcal{I} where is performed the global sensitivity analysis presented in the section 3.

diffusive regime for $R \ll 1$ and gives $\gamma_0 = -\nu k_0^2$. Therefore, we show in the figure 3 how the initial conditions of the DNS database are distributed among the inertial or diffusive regimes. At large Reynolds number, $R > 10$, the influence of the diffusion D is weak and the linear growth rate scaling corresponds to the inertial limit with $\gamma_0^* = R^{-1/3}$. Similarly, a significant amount of simulations are diffusive with $\gamma_0^* = -R^{-4/3}$. Depending on B , part or all of the modes are linearly stable. The remaining simulations are distributed in the intermediate range between the neutral stability curve and the maximum growth rate as shown in the figure 3. It is also important to stress that this analysis does not account for the steepness parameter S , indicating, when it is large, that the non-linear effects are already significant. In addition, the perturbation, through parameter S , artificially increases the effective diffusion thickness such that the linear growth rate is further damped.

2.3. The dynamics of the 0D quantities

To examine the dynamics of the Rayleigh-Taylor Instability (RTI), we focus on the zero-dimensional (0D) turbulent quantities derived from averaging across the entire width of the mixing layer, which are commonly utilized in mix models.

Given that the RTI is statistically homogeneous in the horizontal (x, y) plane, it is practical to introduce the horizontal average \bar{Q} and the fluctuation q of a quantity Q , as determined by the Reynolds decomposition $Q = \bar{Q} + q$. Within the context of the Boussinesq approximation, the RTI exhibits a zero mean velocity, $\bar{\mathbf{u}} = 0$. Moreover, the concentration field can be expressed as $C(\mathbf{x}, t) = \bar{C}(z, t) + c(\mathbf{x}, t)$, allowing to define the mixing zone size as (Andrews & Spalding 1990)

$$L = 6 \int_{-\infty}^{+\infty} \bar{C}(1 - \bar{C}) dz. \quad (2.7)$$

This definition for L , Eq. (2.7), derives from a piecewise mean concentration profile that

accurately represents a turbulent Rayleigh-Taylor mixing zone. Notably, for a diffuse interface without perturbation, L is equivalent to δ from Eq. (2.2).

To more accurately characterize the velocity field \mathbf{u} , this study considers the 0D turbulent kinetic energy \mathcal{K} and its dissipation ε

$$\mathcal{K} = \frac{1}{L} \int_{-\infty}^{+\infty} \frac{1}{2} \overline{\mathbf{u} \cdot \mathbf{u}} dz, \text{ and } \varepsilon = \frac{1}{L} \int_{-\infty}^{+\infty} \nu \overline{\nabla \mathbf{u} : \nabla \mathbf{u}} dz. \quad (2.8a)$$

Similarly, concentration fluctuations c are captured by the scalar variance \mathcal{K}_{cc} and the scalar dissipation ε_{cc} ,

$$\mathcal{K}_{cc} = \frac{1}{L} \int_{-\infty}^{+\infty} \overline{c^2} dz, \text{ and } \varepsilon_{cc} = \frac{1}{L} \int_{-\infty}^{+\infty} 2\kappa \overline{\nabla c \cdot \nabla c} dz. \quad (2.8b)$$

Additionally, the global mixing parameter Θ is considered as an alternative representation to \mathcal{K}_{cc} (Young *et al.* 2001)

$$\Theta = \frac{\int_{-\infty}^{+\infty} \overline{C(1-C)} dz}{\int_{-\infty}^{+\infty} \overline{C(1-C)} dz} = 1 - 6\mathcal{K}_{cc}. \quad (2.8c)$$

The system is further characterized by the vertical concentration flux \mathcal{F} , which signifies the injection of potential energy. The growth rate of the mixing layer and the elongation of density structures along the vertical direction are quantified by the self-similar coefficient α and the dimensionality parameter $\sin^2(\Gamma)$, respectively

$$\mathcal{F} = \frac{1}{L} \int_{-\infty}^{+\infty} \overline{u_z c} dz, \quad \alpha = \frac{(\dot{L})^2}{8\mathcal{A}gL}, \text{ and } \sin^2(\Gamma) = \frac{\int_0^\pi \sin^2(\theta) \mathcal{E}_{cc} \sin(\theta) d\theta}{\int_0^\pi \mathcal{E}_{cc} \sin(\theta) d\theta}, \quad (2.8d)$$

where $\mathcal{E}_{cc}(\theta, t)$ is the concentration covariance spectra in spherical coordinates integrated along the radial and azimuthal coordinates.

The 0D quantities are interconnected, as illustrated by the budget equations for kinetic energy and scalar variance

$$\left(\frac{d}{dt} + \frac{\dot{L}}{L} \right) \mathcal{K} + 2\mathcal{A}g\mathcal{F} + \varepsilon = 0, \quad (2.9a)$$

$$\left(\frac{d}{dt} + \frac{\dot{L}}{L} \right) \mathcal{K}_{cc} + 2\frac{\mathcal{F}}{L} + \varepsilon_{cc} = 0. \quad (2.9b)$$

Noticeably, while the budget equation for kinetic energy, Eq. (2.9a), is exact, the equation for the scalar, Eq. (2.9b), relies on an uniform mean concentration gradient inside the mixing layer.

The mixing zone size L and all the other 0D quantities \dot{L} , \mathcal{K} , ε , Θ , ε_{cc} , \mathcal{F} , $\sin^2(\Gamma)$ and α are computed in the various DNS simulations at all times. In order to investigate the RTI phenomenology and to shed light on the transition to turbulence, it is important to work with non-dimensional state variables. This is done by using the viscosity ν and the buoyancy acceleration $\mathcal{A}g$ to rescale the time and the length. The non-dimensional quantities are thus marked with a star \star symbol such that for instance $t^\star = t(\mathcal{A}g)^{2/3}/\nu^{1/3}$ and $L^\star = L(\mathcal{A}g)^{1/3}/\nu^{2/3}$.

The Rayleigh-Taylor simulations are stopped, either when the mixing zone width reaches half of the vertical computational domain (*i.e.* $L \geq 2\pi$), or when the integral scale of turbulence becomes too large. This latter condition is defined from the 0D quantities as $\ell_I = \mathcal{K}^{3/2}/\varepsilon > 3\pi/10$, or equivalently in term of wavenumber $k_I = 2\pi/\ell_I < 6.7$.

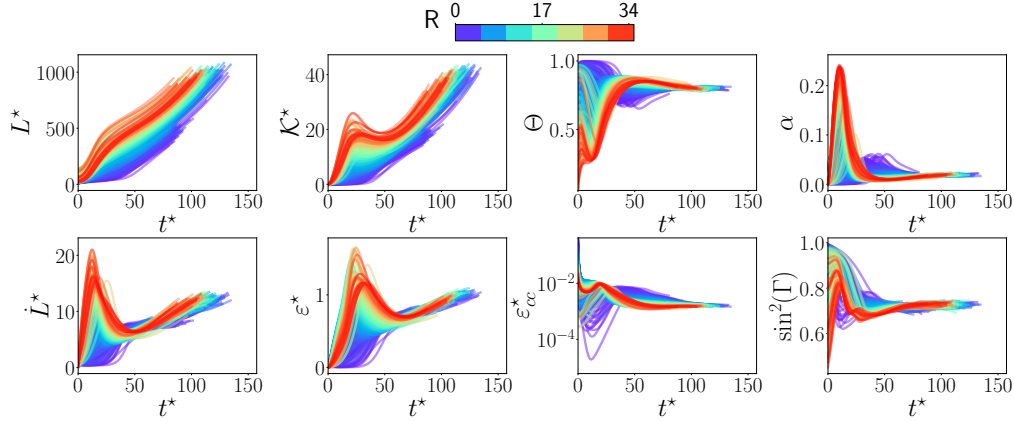


Figure 4: Time evolution of the 0D quantities L , \dot{L} , \mathcal{K} , ε , Θ , ε_{cc} , \mathcal{F} and α evaluated for all the RT DNS. The trajectories are colourized as a function of the initial Reynolds number R .

In practice, it is mainly the criterion on the integral scale which determines the end of the simulations. This procedure aims at reducing the risk of the lateral confinement of the large eddies which would alter the growth of the mixing layer.

We now discuss the dynamics of the 0D quantities computed from the DNS, that are presented in the figure 4. The fact that the simulations end at different values of t^* is not only the consequence of the stop criterion detailed before, but also to the non-dimensionalization procedure as inertial trajectories with small initial Reynolds number for instance are run with a small buoyancy acceleration Ag .

A large dispersion of the mixing zone width is observed among the DNS due to the initial conditions. The figure 4 highlights the importance of the Reynolds number which, as expected, mainly selects between inertial or diffusive behaviours. The diffusion D , the steepness S and the spectral bandwidth B also play a role which will be investigated later in the part 3. Before detailing how the trajectories differ, we remark that most of them reach the self-similar regime. This is characterized by a quadratic growth in time for L^* and \mathcal{K}^* , a linear growth for \dot{L}^* , $-\mathcal{F}^*$ and ε^* and a constant for the global mixing and dimensionality parameters Θ and $\sin^2(\Gamma)$, the coefficient α and the scalar dissipation ε_{cc}^* . In particular, the values for the self-similar coefficient and for the global mixing parameter collected at the end of the simulations are $\alpha = 0.019 \pm 0.002$ and $\Theta = 0.80 \pm 0.008$ which are consistent with the usual DNS results. This is also well consistent with a self-similar regime driven by a mode coupling phenomenology as explained in Dimonte (2004). However, depending on how large is the initial bandwidth B , mode competition effects can also take place during the transients.

We now compare more specifically an inertial and a diffusive DNS in the figure 5. The diffusive trajectory having a smaller linear growth, even negative for some modes, the convergence toward the self-similar regime is therefore delayed with respect to the inertial configuration. The transition to turbulence is very rapid in the inertial case, occurring around the peak of ε^* at $t^* = 20$. This transition, associated to the secondary instabilities between bubbles and spikes, also corresponds to an increase of the global mixing parameter Θ . It leads to a diminution of the mixing layer growth as shown by

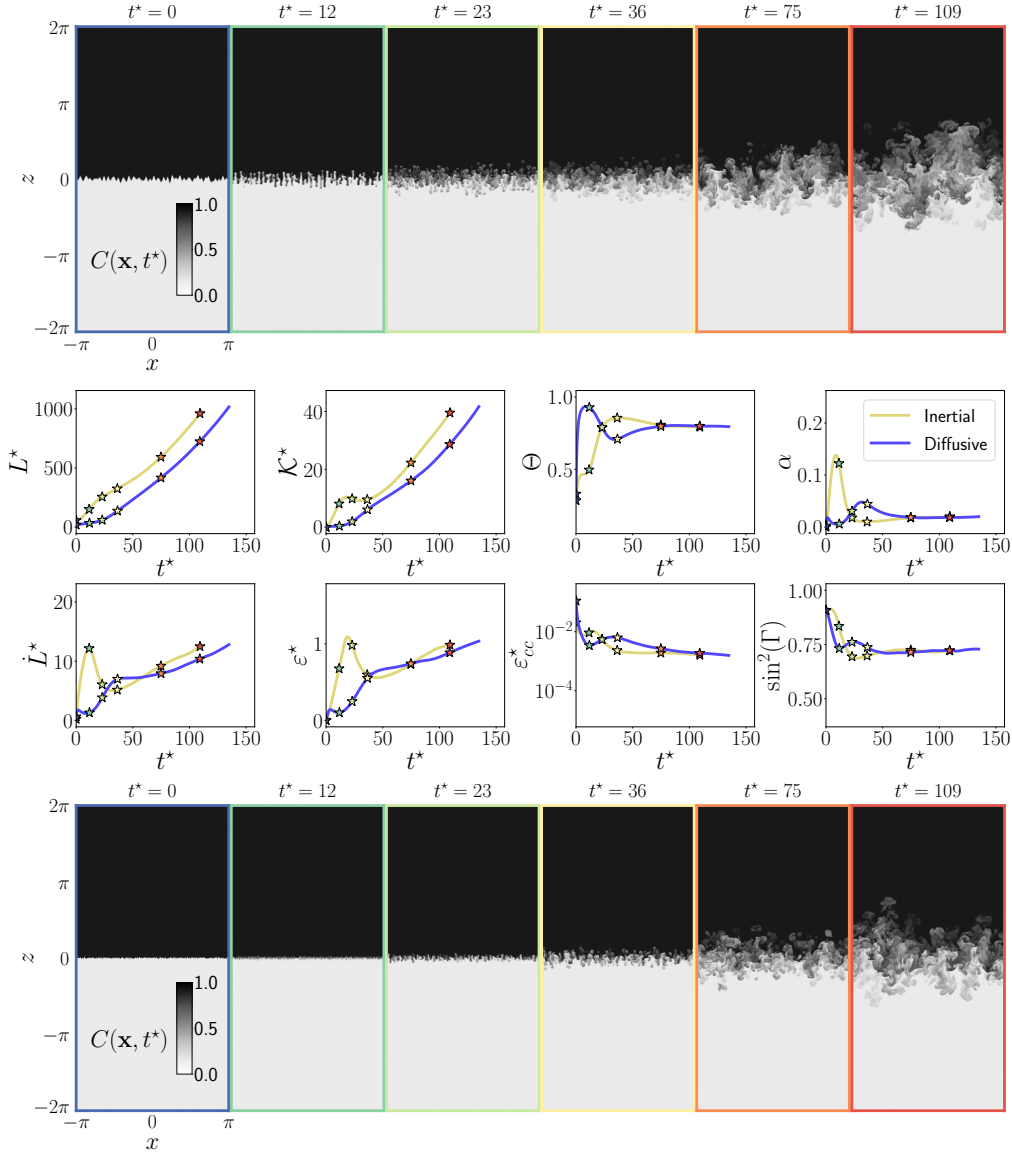


Figure 5: (Top): 2D slices at different times of the concentration field C extracted from a DNS corresponding to an inertial configuration with $R = 12.5$, $B = 0.14$, $S = 3.0$ and $D = 3.0$. (Bottom): Same but for a diffusive case with $R = 2.35$, $B = 0.14$, $S = 3.0$ and $D = 3.0$. (Middle): Time evolution of the 0D quantities for the inertial and diffusive trajectories. The star symbols indicate the times of the 2D concentration slices presented in the figure. The plain curves are dashed when the integral scale corresponding to the stop criterion detailed in the section 2.3 becomes too large.

the formula provided by the rapid acceleration model (Gréa 2013)

$$\alpha = \frac{\sin^4(\Gamma)(1 - \Theta)^2}{1 + \sin^2(\Gamma)(1 - \Theta)} \quad \text{with} \quad \frac{2}{3} \leq \sin^2(\Gamma) \leq 1, \quad (2.10)$$

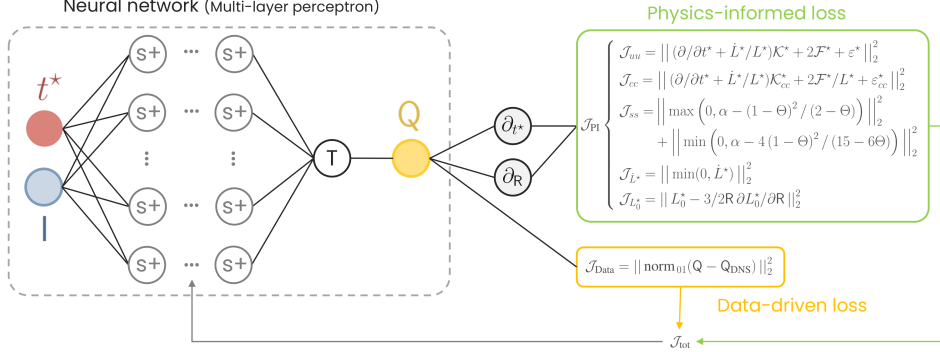


Figure 6: Depiction of the physics-informed neural network as a surrogate for modelling the DNS’s 0D quantities. The total loss consists of a data-driven component, $\mathcal{J}_{\text{Data}}$, aiming to minimize the discrepancy between the neural network and DNS outputs, and a physics-informed component, \mathcal{J}_{PI} , formulated via automatic differentiation and assessed at new collocation points. This approach enhances the conservation of kinetic energy and scalar variance balances, enforces a constraint on α , ensures \dot{L}^* remains positive, and upholds the consistency of L_0^* .

where $\sin^2(\Gamma) = 1$ for purely vertical structures. By contrast, it seems more progressive and delayed in the diffusive configuration where it becomes less convenient to define a clear transition time.

2.4. A physics-informed surrogate model for the RT simulations

Although the DNS contain ample information for exploring the memory of the RTI, their significant computational demands render them impractical for analyses requiring extensive evaluations. To facilitate global sensitivity analysis and the resolution of Bayesian inverse problems, it becomes advantageous to develop a surrogate model of our DNS database.

This surrogate model must be sufficiently precise to ensure the validity of our conclusions. Given the voluminous DNS data and the problem’s high degree of nonlinearity, neural networks (NNs) appear particularly well-suited for this purpose. In recent years, NNs have been employed in numerous turbulent flow studies (Ling *et al.* 2016; Brunton *et al.* 2019; Duraisamy *et al.* 2019; Guastoni *et al.* 2021; Buaria & Sreenivasan 2023; Solera-Rico *et al.* 2024; Zhu *et al.* 2024), demonstrating their capacity to tackle complex fluid mechanics challenges. In this study, the NN surrogate model aids in elucidating the impact of initial conditions, pinpointing critical moments of the transition to turbulence, and identifying key quantities for monitoring.

Accordingly, the NN surrogate model maps the time t^* and the initial conditions $l = (R, B, S, D)^T$ to the 0D quantities $Q = (L^*, \dot{L}^*, \mathcal{K}^*, \varepsilon^*, \Theta, \varepsilon_{cc}^*, \mathcal{F}^*, \sin^2(\Gamma))^T$ as outputs (see the figure 6). This scenario is relatively straightforward since the DNS trajectories are distinctly defined by four dimensionless initial parameters. A simple multi-layer perceptron architecture suffices for creating an initial model that accurately links the five inputs to the seven outputs (with \dot{L}^* determined through auto-differentiation). This architecture is crafted to reinforce the self-similar scaling laws of various 0D quantities for extensive t^* values (see appendix A for more details).

In order to improve the quality and the robustness of the surrogate model, we try to

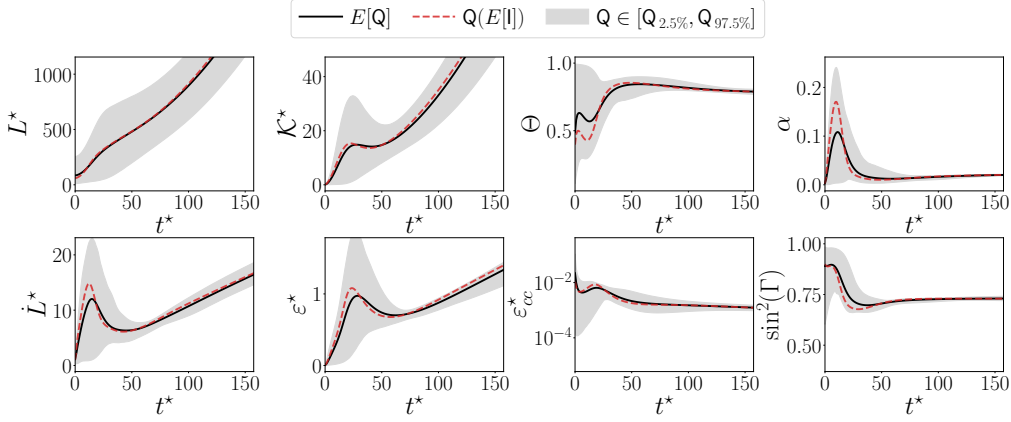


Figure 7: Evolution and dispersion of the 0D trajectories $q(t^*; \mathbf{l} \in \mathcal{I})$ with initial conditions following the joint prior distribution in the extended domain \mathcal{I} . The mean trajectories $E[q]$ are represented in plain line and in dashed line is the trajectory corresponding to the mean of the initial conditions $q(t^*; E[\mathbf{l}])$. The shaded areas indicate the zones delimited by the variance $V[q]$ or the 95% confidence interval.

enforce several physical properties through unsupervised terms in the loss function: (i) $\dot{L}^* \geq 0$ as the acceleration is always destabilizing, (ii) the conservation of the kinetic and potential energy budgets Eqs. (2.9a)-(2.9b), (iii) the self-similar relation between α and Θ provided by Eq. (2.10), and (iv) the dimensional relation $L_0^* = 3/2R \partial L_0^* / \partial R$ expressing the fact that the initial mixing zone width does not depend on the acceleration (or R). Consequently, the NN emerges from a physics-informed machine learning methodology (Karniadakis *et al.* 2021).

Incorporating these properties not only bolsters the model’s resilience—especially in data-sparse regions—but also boosts confidence in the model as it aligns more closely with fundamental physics principles, offering credible solutions.

3. Sensitivity analysis

In this section, we aim to assess how the initial parameters $\mathbf{l} = (R, B, S, D)^T$ influence the 0D quantities. To achieve this, we utilize the surrogate model introduced in Section 2.4 to rapidly evaluate the dynamics and quantify the sensitivity to the initial conditions. This global approach involves sampling the initial conditions across an extended region of the initial parameter space \mathcal{I} , as defined below (also see the figures 2 and 3):

$$R \in [0.2, 35], B \in [10^{-2}, 1.7], S \in [0.5, 10], \text{ and } D \in [0.7, 20]. \quad (3.1)$$

Within this domain, \mathbf{l} is sampled using a joint prior distribution, $p(\mathbf{l})$, which is uniform for R and B , and log-uniform for S and D . This ensures coverage of both inertial and diffusive trajectories. Initially, we present a comprehensive overview of the dependency on \mathbf{l} , subsequently focusing more specifically on the late time self-similar dynamics. The final part is dedicated to the conditional sensitivity analysis at a given initial mixing zone L_0^* .

3.1. Main effect of the initial conditions

The figures 7 and 8 detail how the various 0D quantities q , parametrized by the initial conditions \mathbf{l} , evolve and vary. A considerable dispersion of trajectories is observed,

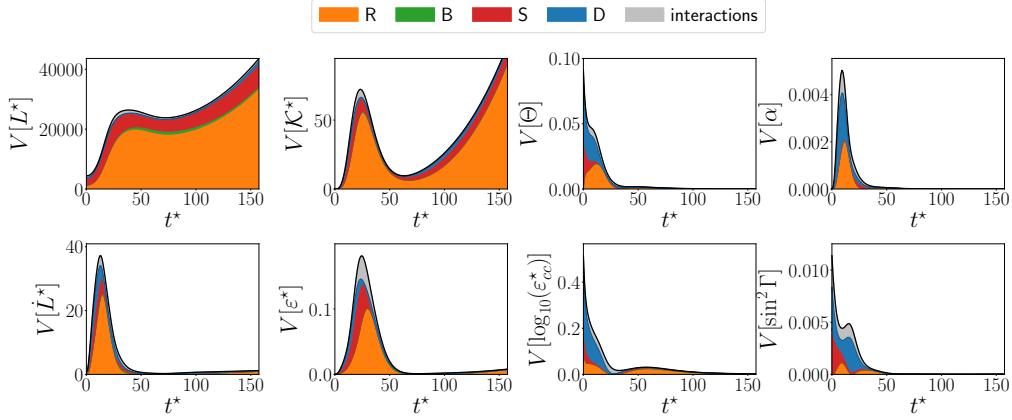


Figure 8: Evolution of the variances for the 0D trajectories, $V[q(t^*; \mathbf{l} \in \mathcal{I})]$, with initial conditions sampled with the prior distribution in the extended domain \mathcal{I} . The first order Sobol indices s_i^q are computed in order to disentangle the initial condition effects. Their respective contributions are indicated by the coloured areas of width $s_i^q V[q(t^*; \mathbf{l})]$ in the figure.

especially for the mixing width L^* . This highlights the challenge in modelling Rayleigh-Taylor turbulence, which remains highly sensitive to the unknown initial conditions. The variance of the mixing zone $V[L^*]$ —represented by the shaded area width accompanying the trajectories—is primarily driven by the diversity in initial mixing zone values, L_0^* . However, the pronounced variance is chiefly attributed to the linear growth rates, which are highly sensitive to \mathbf{l} as indicated by Eq. (2.6). Therefore, the variance exponentially grows until the transition to turbulence around $t^* \in [25, 50]$. When entering the self-similar regime at late time, the variance is still growing accompanying the mixing zone evolution. By contrast, the variance of \dot{L}^* remains very small in the self-similar regime, echoing a nearly constant value for the self-similar parameter α at late time shown in the figure 7. This pattern aligns with Eq. (2.10), as the mixing and dimensionality parameters, Θ and $\sin^2(\Gamma)$, also tend toward constant values. The variance of the vertical concentration flux $V[\mathcal{F}^*]$ (not shown) mirrors the trend of $V[\dot{L}^*]$ since both quantities are nearly proportional within the 0D equations. The kinetic energy variance $V[K^*]$ is anticipated to follow a scaling law similar to $V[(\dot{L}^*)^2]$. Nonetheless, a significant variation occurs around $t^* = 25$, aligning with the onset of turbulence. This assertion is corroborated by the peak in the dissipation variance $V[\epsilon^*]$, coinciding with the emergence of secondary Kelvin-Helmholtz instabilities. With the scalar dissipation ϵ_{cc}^* diminishing as $1/t^*$ in the self-similar regime, its variance also rapidly decreases. Due to the non-linear dependency on \mathbf{l} , generally, $E[q(t^*; \mathbf{l})] \neq q(t^*; E[\mathbf{l}])$.

To pinpoint the initial conditions' influence, we calculate the temporal evolution of the first-order Sobol indices s_i^q , also known as the main effects, with $i \in \{R, B, S, D\}$ which, for a quantity q , are defined as (see appendix B)

$$s_i^q = \frac{V[E[q|i]]}{V[q]}. \quad (3.2)$$

The Sobol indices thus depend on the joint prior distribution $p(\mathbf{l})$ taken in the extended domain \mathcal{I} , Eq. (3.1). A large Sobol index s_i^q indicates an important sensitivity to the parameter i . It can be verified that $\sum_i s_i^q \leq 1$, with equality when initial conditions effects

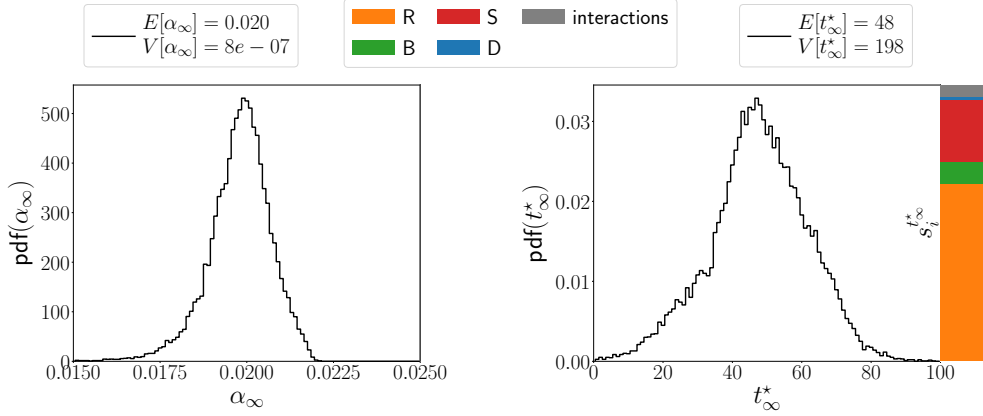


Figure 9: Probability density functions (PDFs) for α_∞ and t_∞^* using the surrogate model, with initial conditions \mathcal{I} sampled in the extended domain Eq. (3.1). The mean and the variance are indicated in the legend. The first-order Sobol indices $s_i^{t_\infty^*}$ are also plotted.

are decoupled. In the figure 8, we see that the variance of each 0D quantity is correctly captured by the first Sobol indices. The coupling between the parameters, expressed by the values of the higher order Sobol indices, becomes more significant around the transition to turbulence, $t^* \approx 25$. It comes as no surprise that the transition regime is the most complex phase to model the RT dynamics. Noticeably, the 0D quantities are very sensitive to the Reynolds number R mainly controlling the growth of the layer. The steepness S has also its importance, in particular to explain the variability of L^* . The diffusive parameter D also plays a role in the global mixing parameter Θ variability, in particular during the first stage of the instability. This is of course expected as a very diffused layer leads to higher Θ . Consequently, it mainly appears in the initial α variance from Eq. (2.10). The parameter B expressing the band width seems to have a limited effect on the variability of the 0D quantities in the domain we considered. However and according to linear stability analysis, for an initial condition having a mean wavenumber growth rate around zero, a larger bandwidth has more chances to have at least one unstable mode, which leads to a very different dynamics. So the parameter B has a strong influence in this case, in a reduced domain at low R .

3.2. Late time sensitivity to initial conditions

At late times, trajectories are expected to follow self-similarity, hence being solutions to a buoyancy-drag equation, as demonstrated in previous studies (Fermi & von Newman 1951; Ramshaw 1998; Ristorcelli & Clark 2004; Cook & Cabot 2006; Boffetta *et al.* 2011):

$$L^* = 2\alpha_\infty(t^* + t_\infty^*)^2, \quad (3.3)$$

where α_∞ denotes an asymptotic growth rate, and t_∞^* a virtual origin that aligns self-similar trajectories. We may compute the values of α_∞ and t_∞^* by fitting Eq. (3.3) over a late time interval. We consider for instance $t^* \in [160, 170]$, such that the DNS trajectories are in the self-similar regime while the surrogate model is not too much extrapolating (the results shown hereafter are not sensitive to this interval choice). By sampling again the initial conditions on the extended domain \mathcal{I} Eq. (3.1), we obtain the pdf for α_∞ and t_∞^* in the figure 9.

The α_∞ values cluster tightly around their mean $E[\alpha_\infty] = 0.020$, with minimal variance

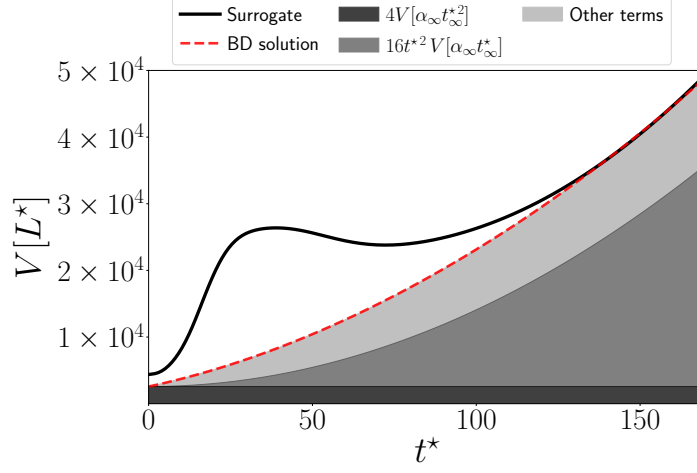


Figure 10: Time evolution of $V[L^*]$, evaluated using the neural network surrogate model with initial conditions sampled within the extended domain \mathcal{I} (solid line). The variance, reconstructed from the buoyancy-drag (BD) solution (Eq. (3.3)), appears in dashed lines, further broken down into contributions from variations in α_∞ and t_∞ .

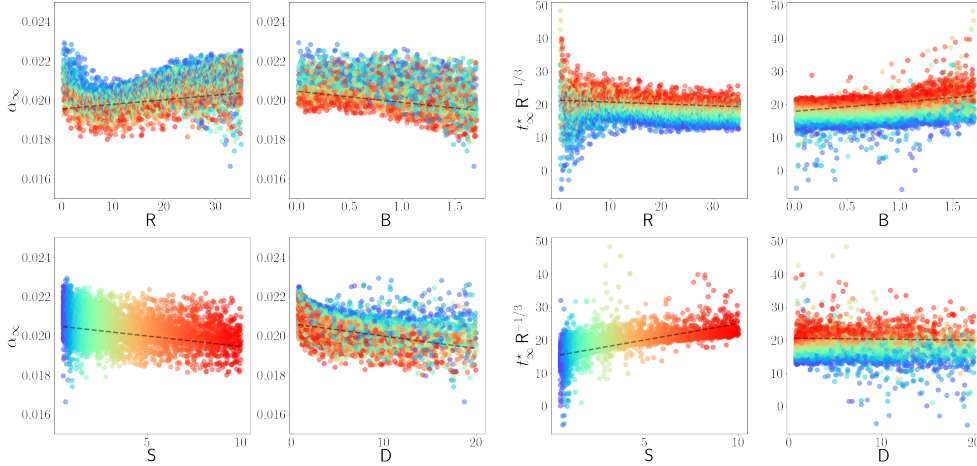


Figure 11: Values of α_∞ and t_∞^* sampled over a log uniform distribution of the initial parameters \mathcal{I} . The symbols associated to the trajectories are coloured by the steepness S .

within $\alpha_\infty \in [0.019, 0.021]$, aligning with findings from DNS analyses (see Section 2.3). Conversely, t_∞^* exhibits a broader dispersion, ranging from $t_\infty^* \in [10, 90]$ with a mean $E[t_\infty^*] = 48$. Thus, in the self-similar regime, t_∞^* variations predominantly govern $V[L^*]$ variance. This hypothesis is corroborated by utilizing Eq. (3.3) and the pdf for α_∞ and t_∞^* to reconstruct the variance for L^* . The results are presented in the figure 10.

At late times, the reconstructed variance aligns with the true variance of L^* . Decomposing Eq. (3.3) reveals that $V[L^*] \approx (t^*)^2 V[\alpha_\infty t_\infty^*]$. Variations in α_∞ , potentially causing a variance growth proportional to $(t^*)^4$, exert minimal influence on trajectory dispersion within this time frame.

In the figure 9, we also analyse t_∞^* 's dependency on l through Sobol indices. Given the negligible variance in α_∞ , possibly attributable to the surrogate model's precision, we abstain from inferring physical significance from these fluctuations. Besides at late time, the turbulent mixing zone growth is determined by the very anisotropic structures at large scales. Therefore the viscosity ν , or equivalently R , should not play an important role in the self-similar dynamics. This explains why a constant α_∞ is expected and that $t_\infty^* \propto R^{1/3}$ from dimensional analysis, as evidenced by the large value of $s_R^{t_\infty^*}$. In the figure 11, we present the sampled characteristics of the asymptotic regimes. The distributions of α_∞ and $t_\infty^* R^{-1/3}$ have a very small dependence on R confirming that the viscosity does not play a role in the late time regime. Still we observe a small dependence on R which can be attributed to the diffusive trajectories. Moreover, the large Sobol indices $s_S^{t_\infty^*}$ shed light on the importance of the steepness S on the late-time regime. This trend is more explicitly observed in the figure 11. Therefore, t_∞^* sensitively increases with S . In addition, the results show some dependence on the band width B and to a lesser degree on the diffusion number D . We thus propose a linear fit for α_∞ and t_∞^* which allows to evaluate the impact of the initial default of an interface on the late time dynamics. This leads to

$$\begin{cases} \alpha_\infty \simeq 0.021 + (2.3 R - 56 B - 11 S - 6.3 D) \times 10^{-5}, \\ t_\infty^* \simeq R^{1/3}(13.94 - 0.05 R + 2.79 B + 1.00 S - 0.03 D). \end{cases} \quad (3.4)$$

The formula (3.4) confirms the importance of R , S , and to a lesser degree on D . The strong coefficient associated to B has to be contrasted with its domain of definition, $B \in [0, 2]$, so it has a weak effect on the self-similar dynamics. The virtual origin derives from the early RT dynamics, including the transition to turbulence. It is thus larger when the initial mixing layer growth is important. The effect of S cannot be provided by the linear theory as it is only valid in the limit $S \rightarrow 0$. Still, we can consider the rapid acceleration model exhibiting a buoyancy drag equation parametrized by the turbulence quantities (Gréa 2013). Initially the growth is mainly controlled by the buoyancy coefficient which is provided by the global mixing parameter and the dimensionality coefficient as $\sin^2(\Gamma)(1 - \Theta)$. A large steepness S will generate more elongated structure (or large $\sin^2(\Gamma)$) and less mixing (smaller Θ). It results strong buoyancy effects and therefore larger t_∞^* in the self-similar regime. Conversely, the dependence of the late time t_∞^* to S and B can also be related to the presence of mode competition phenomenology during the transient (Dimonte 2004). Therefore, a large steepness parameter S reduces the Fermi transition time, *i.e.* the time at which a mode saturates and reaches its terminal velocity, leading to larger t_∞^* .

3.3. Sensitivity analysis conditioned at a given L_0^*

Thus far, our investigation has covered the global effects of the initial parameters l on RT dynamics. While the initial conditions are often unknown, the initial mixing zone width L_0^* is usually measurable. Therefore, conducting a sensitivity analysis at a specific L_0^* is worthwhile.

Firstly, it is beneficial to determine how L_0^* relates to the initial conditions. Through various approximations, we derive:

$$L_0^* \approx R^{2/3} F(S, D), \quad (3.5)$$

with $F = k_0 L_0 = D$ when $S \ll D$ and $F \simeq 3S$ when $S \gg D$. We also verified that L_0^* was weakly dependent on B .

We present in the figure 12 the conditional pdf of α_∞ and t_∞^* characterizing the late

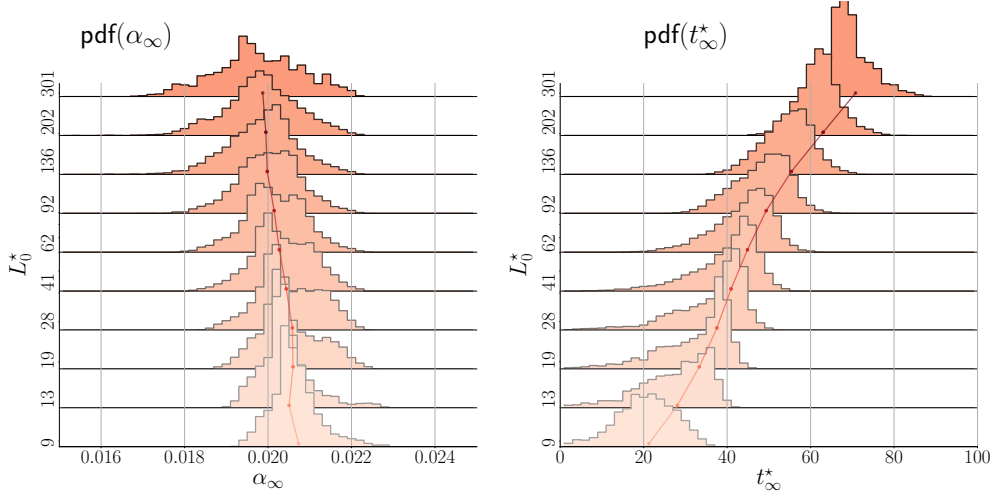


Figure 12: Conditional probability density functions for α_∞ (Left) and t_∞^* (Right) given L_0^* . The initial conditions \mathcal{I} are sampled using the joint prior distribution. The plain lines show the evolutions of $E[\alpha_\infty | L_0^*]$ and $E[t_\infty^* | L_0^*]$.

time dynamics at given L_0^* . Compared to the unconditional pdf presented in the figure 9, the knowledge of L_0^* reduces the uncertainties while not completely eliminating them. Besides, we observe a very small dependence of $E[\alpha_\infty | L_0^*]$ to L_0^* , while the dependence of $E[t_\infty^* | L_0^*]$ to L_0^* is more pronounced, which can be interpreted using Eq. (3.5). For small L_0^* , the dispersion on R and S is reduced such that the dispersion on α_∞ and t_∞^* are limited compared to larger L_0^* . As L_0^* grows, so are R and S such that we observe a slight diminution of α_∞ and growth of t_∞^* as detailed by Eq. (3.4). Therefore, assuming S, D and B are fixed, then we can expect $t_\infty^* \sim (L_0^*)^{1/2}$ (valid for inertial trajectories).

4. Inferring the initial conditions of Rayleigh-Taylor turbulence

We have explored how 0D quantities respond to the initial conditions \mathbf{l} , particularly highlighting the self-similar regime. The enduring impact of the initial conditions on late-time dynamics serves as a memory of Rayleigh-Taylor turbulence. We continue this analysis by identifying the initial conditions \mathbf{l} and the time t^* at which 0D quantities are measured. Our goal is to assess how well these 0D quantities retain the memory of Rayleigh-Taylor turbulence and their predictive capability regarding the mixing zone's future dynamics. We frame the issue within the context of classical Bayesian inference, subsequently examining how the memory of initial conditions diminishes across successive RTI stages for two sets of 0D variables.

4.1. Problem formulation

Here we assume we have knowledge of a 0D vector \mathbf{Q} (for instance with two variables $\mathbf{Q}_2 = (L^*, \dot{L}^*)^T$) and seek to find the initial conditions \mathbf{l} and time t^* corresponding to this measurement. In a Bayesian formulation, this involves computing the joint posterior distribution $p(\mathbf{l}, t^* | \mathbf{Q})$ which, according to Bayes rule, is expressed as

$$p(\mathbf{l}, t^* | \mathbf{Q}) = \frac{p(\mathbf{Q} | \mathbf{l}, t^*) p(\mathbf{l}, t^*)}{p(\mathbf{Q})}. \quad (4.1)$$

In the equation (4.1), $p(\mathbf{Q}|\mathbf{l}, t^*)$ classically defines the likelihood, $p(\mathbf{l}, t^*)$ the joint prior and $p(\mathbf{Q})$ the marginal distribution.

To determine the posterior distribution from Eq. (4.1), we first need to specify the joint prior $p(\mathbf{l}, t^*)$ which we would like as less informative as possible. The analysis relies on the ability of the surrogate model to correctly predict the RT trajectories, so we do not want to use it in extrapolation. The joint prior distribution is therefore non zero only for $(\mathbf{l}, t^*) \in \mathcal{I} \times [0, 150]$ where the surrogate model is well representative of the DNS. This domain corresponds to the white area in the figure 2, bounded in black for the minimum and maximum values. In this 5-dimensional domain, the prior is taken to be uniform in \mathbf{R} , \mathbf{B} , t^* and log uniform in \mathbf{S} , \mathbf{D} , consistent with the sensitivity analysis proposed in the section 3.

The joint likelihood is obtained from a multivariate normal distribution, $\mathcal{N}(\hat{\mathbf{Q}}(t^*; \mathbf{l}), \boldsymbol{\Sigma})$, where the mean is obtained from the neural network surrogate model $\hat{\mathbf{Q}}(t^*; \mathbf{l})$ and the covariance matrix is chosen diagonal, $\boldsymbol{\Sigma} = \boldsymbol{\sigma}\mathbf{I}$, with the variances $\boldsymbol{\sigma}$ evaluated from the error between the surrogate model and the DNS database. So the likelihood is defined as

$$p(\mathbf{Q}|\mathbf{l}, t^*) = \frac{1}{(2\pi)^{N_{\mathbf{Q}}/2} |\boldsymbol{\Sigma}|^{1/2}} \exp \left[-\frac{1}{2} (\hat{\mathbf{Q}}(t^*; \mathbf{l}) - \mathbf{Q})^T \boldsymbol{\Sigma}^{-1} (\hat{\mathbf{Q}}(t^*; \mathbf{l}) - \mathbf{Q}) \right], \quad (4.2)$$

where $N_{\mathbf{Q}}$ is the dimension of the 0D vector \mathbf{Q} considered.

Due to the high computational cost of evaluating the marginal distribution in a high-dimensional space, as $p(\mathbf{Q}) = \int p(\mathbf{Q}|\mathbf{l}, t^*) p(\mathbf{l}, t^*) d\mathbf{l} dt^*$, the rapid evaluation of the likelihood with the surrogate model allows us to employ a Markov Chain Monte-Carlo (MCMC) method to sample the posterior distribution (Metropolis *et al.* 1953; Hastings 1970; Gelman *et al.* 2021). Details of the algorithm are provided in Appendix C. Since we anticipate multi-modal posterior distributions in some cases, owing to the inertial or diffusive nature of the trajectories, we use the parallel tempering algorithm to more efficiently explore the parameter space (Geyer 1991; Falcioni & Deem 1999; Sambridge 2014).

4.2. Results

In this part, we apply the Bayesian methodology introduced in Section 4.1 to recover the initial conditions \mathbf{l} and time t^* from both inertial and diffusive trajectories, as depicted in the figure 5. For this purpose, we consider two sets of 0D measurements: $\mathbf{Q}_2 = (L^*, \dot{L}^*)^T$ or $\mathbf{Q}_8 = (L^*, \dot{L}^*, \mathcal{K}^*, \varepsilon^*, \mathcal{F}^*, \varepsilon_{cc}^*, \Theta, \sin^2 \Gamma)^T$. The vector \mathbf{Q}_2 , corresponding to the state variables of a buoyancy-drag model, provides less information compared to \mathbf{Q}_8 , which is roughly associated with more advanced mix models (Olivier Grégoire & Gauthier 2005; Banerjee *et al.* 2010; Schwarzkopf *et al.* 2011; Morgan & Wickett 2015; Schilling & Mueschke 2017). Consequently, better inference is expected with \mathbf{Q}_8 .

In the figures 13 and 14, we show the inference results for $\mathbf{Q}_{2,8}$ taken at various times on the inertial and diffusive trajectories. The 5D posterior distributions $p(\mathbf{l}, t^*|\mathbf{Q}_{2,8})$ are here represented by their 2D projections on the planes (t^*, i) (with $i \in \{\mathbf{R}, \mathbf{B}, \mathbf{S}, \mathbf{D}\}$). Globally, the posteriors derived from the full 0D variables \mathbf{Q}_8 performs well to recover the initial conditions \mathbf{l} and the measurement time t^* . By contrast, the inference is degraded when only using the reduced buoyancy-drag variables \mathbf{Q}_2 .

There is of course a correlation between the sensitivity to initial conditions, detailed in the section 3, and the ability to infer these same initial conditions. For instance, the band width \mathbf{B} is not perfectly inferred by both $\mathbf{Q}_{2,8}$ as the trajectories are not very sensitive to this parameter. By contrast, the Reynolds number \mathbf{R} can be well recovered by Bayesian inference, in particular with full knowledge of \mathbf{Q}_8 . At late time, one can notice the correlation between \mathbf{R} and t^* on the posterior distributions. In the self-similar

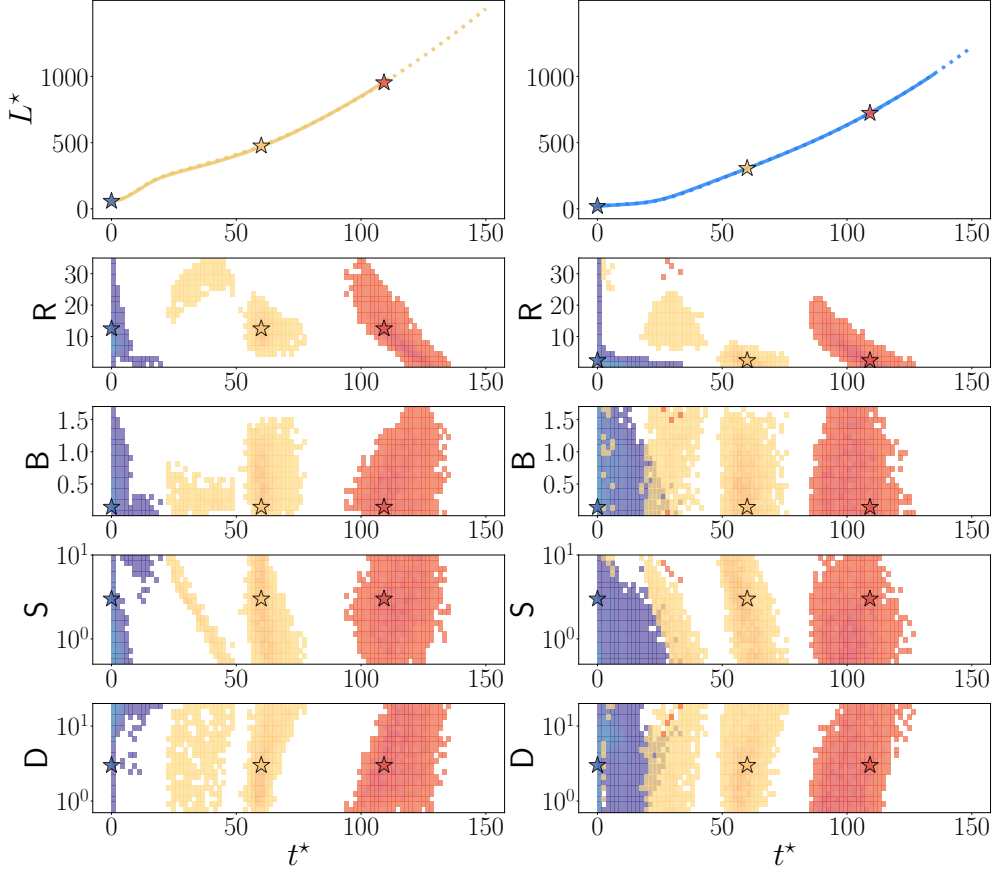


Figure 13: Posterior distributions $p(l, t^* | \mathbf{Q}_2)$ projected on the 2D planes (t^*, i) (with $i \in \{R, B, S, D\}$) and sampled using the MCMC algorithm described in the section 4.1. The three observations \mathbf{Q}_2 corresponding to the buoyancy-drag state vector are taken along (Left) the inertial and (Right) the diffusive RT trajectories introduced in the figure 5 (marked by the star symbols). The plain curves indicate the DNS trajectories and the dashed curve the corresponding neural network surrogate model.

regime, knowing the buoyancy-drag variables \mathbf{Q}_2 gives access to $t^* + t_\infty^*$, as α_∞ is almost constant. Therefore from Eq. (3.4) averaged on the initial domain \mathcal{I} , it is not surprising that the posterior is aligned along $t^* + 21R^{1/3} = 2L^*/\dot{L}^*$ curves as shown in the figure 14.

Inferring the initial conditions from 0D quantities at $t^* = 0$ presents an interesting area of study. With \mathbf{Q}_2 , accurately determining l is not possible. Moreover, t^* is not properly inferred either, the uncertainty resulting from the fact that the state vector \mathbf{Q}_2 is frozen at the beginning of the diffusive trajectories. Conversely, why does \mathbf{Q}_8 perform much better? It can be shown that knowing Θ (or \mathcal{K}_{cc}), ε_{cc}^* and the diffusion coefficient enables the reconstruction of the initial wavenumber k_0 and thus the Reynolds number R .

Noticeably, the figure 13 exhibits multimodal posterior distributions $p(l, t^* | \mathbf{Q}_2)$ when considering the state vector \mathbf{Q}_2 around the transition to the turbulence regime. This phenomenon, appearing in both inertial and diffusive trajectories, makes the evaluation of the posterior challenging and justifies the use of an MCMC parallel tempering algo-

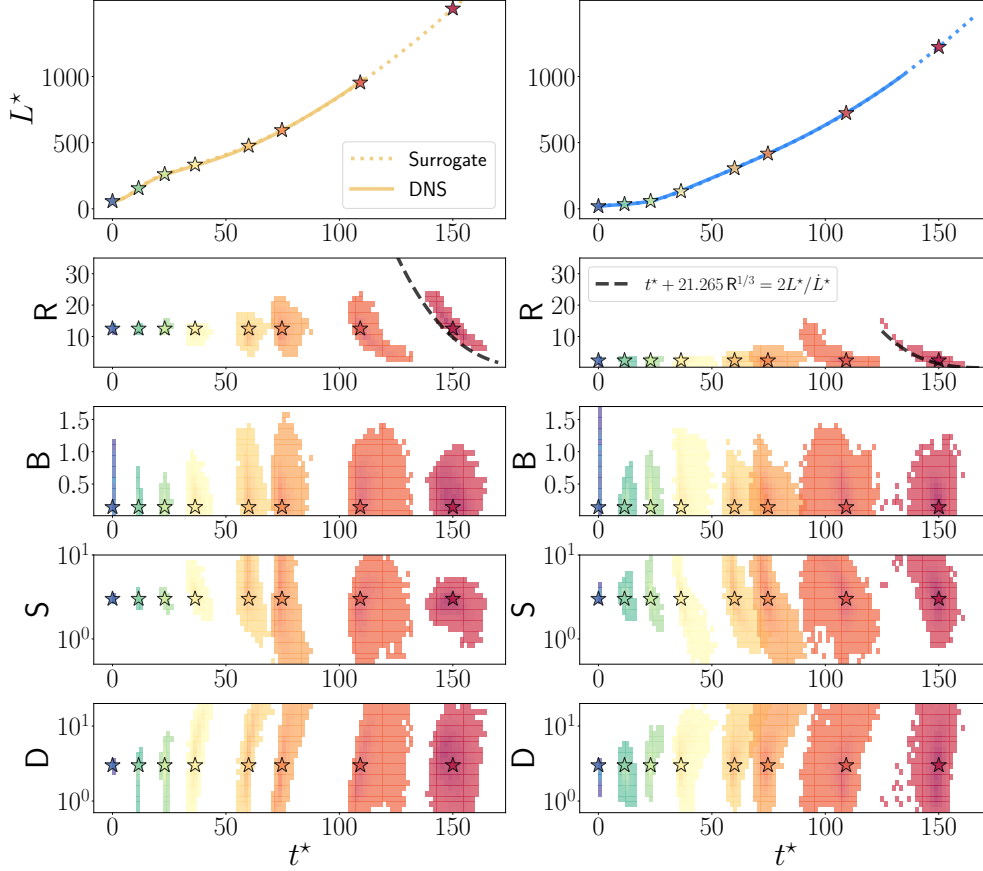


Figure 14: Posterior distributions $p(l, t^* | Q_8)$ projected in the 2D planes (t^*, i) (with $i \in \{R, B, S, D\}$) and sampled using the MCMC algorithm described in the section 4.1. The eight observations Q_8 corresponding to the full 0D state vector are taken along (Left) the inertial and (Right) the diffusive RT trajectories introduced in the figure 5 (marked by the star symbols). The plain curves indicate the DNS trajectories and the dashed curve the corresponding neural network surrogate model. The black dashed lines exhibited in the t^* - R planes come from the sensitivity analysis Eq. (3.4).

rithm. The figure 15 displays the trajectories in the phase plane (L^*, \dot{L}^*) sampled from the posterior distributions. Different trajectories, corresponding here to inertial and diffusive dynamics, converge at the same observation point and cannot be distinguished by knowing Q_2 alone. Conversely, Q_8 enables the differentiation between the various trajectory families, thus leading to more accurate inference. This raises the question: Is it possible to optimize a better set of variables to model the RT dynamics, from the linear to the self-similar regime?

4.3. Finding an optimized state vector for reconstructing the initial conditions

So far we have observed that measuring the full 0D vector Q_8 performs much better for inferring the initial conditions than only the buoyancy-drag variables Q_2 . If a state vector can correctly infer the initial conditions of a trajectory, then it is an excellent candidate for a model. Therefore, it is important to quantify the ability of a state variable Q to

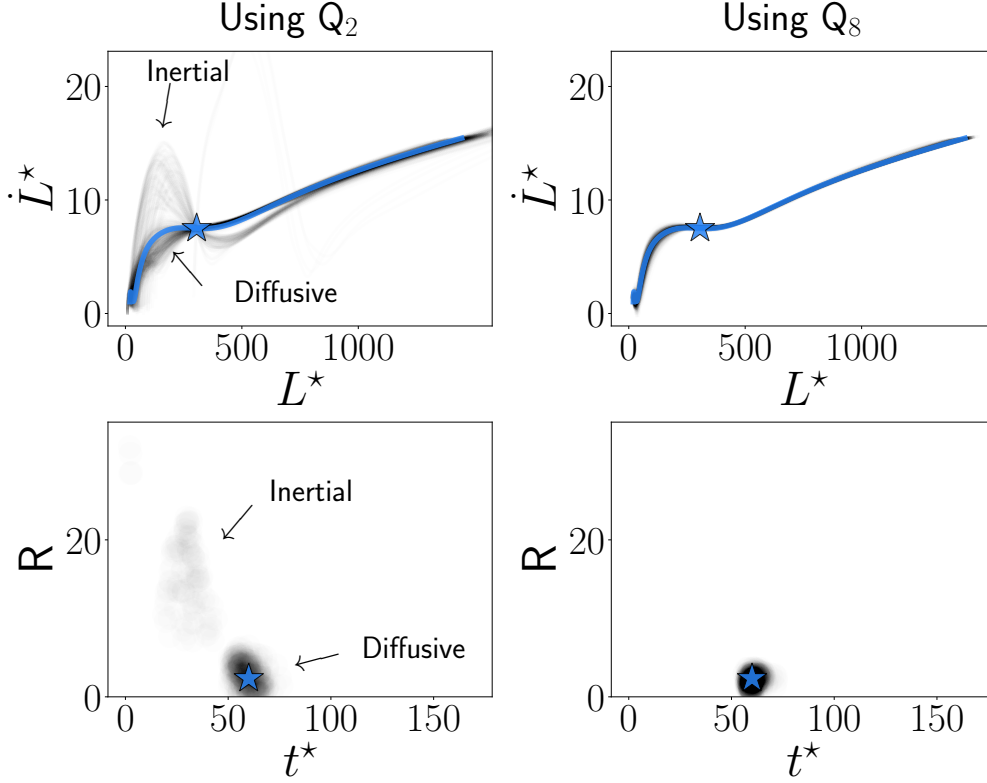


Figure 15: (Top) Trajectories represented in the (L^*, \dot{L}^*) plane and sampled from the joint posterior distributions $p(l, t^* | Q_{2,8})$ projected (Bottom) in the (t^*, R) plane. The figure shows the inference for a diffusive trajectory, where the star symbols in the (L^*, \dot{L}^*) and (t^*, R) planes correspond to the observation, of (Left) Q_2 or (Right) Q_8 .

infer the initial conditions in order to find an optimal set of variables for modelling the full RT dynamics.

Our expectation is to find a posterior distribution close to the initial parameters corresponding to the trajectory we want to reconstruct, *i.e.* $R_{\text{obj}}, B_{\text{obj}}, S_{\text{obj}}, D_{\text{obj}}$ and the measurement time t_{obj}^* . The ability of the posterior to recover the true initial conditions can be evaluated using

$$\mathcal{D}(Q) = \int_{\mathbb{R}^5} \mathcal{D}(t^*, l | Q) p(t^*, l | Q) dl dt^*, \quad (4.3)$$

with

$$\mathcal{D}(t^*, l | Q) = \sqrt{(t^* - t_{\text{obj}}^*)^2 + (R - R_{\text{obj}})^2 + (B - B_{\text{obj}})^2 + (D - D_{\text{obj}})^2 + (S - S_{\text{obj}})^2} \quad (4.4)$$

and where every parameter, t^* , R , B , S and D is normalized between 0 and 1 in order to have the same weight in the measure. In the equation (4.3), the distance is zero if the posterior corresponds to the initial conditions. This measure can be quickly and directly computed from the samples obtained with the MCMC algorithm.

In the figure 16, we present the time evolution of the distance $\mathcal{D}(Q)$ for various 0D quantities taken along the RT inertial trajectory shown in the figure 5. As expected, the

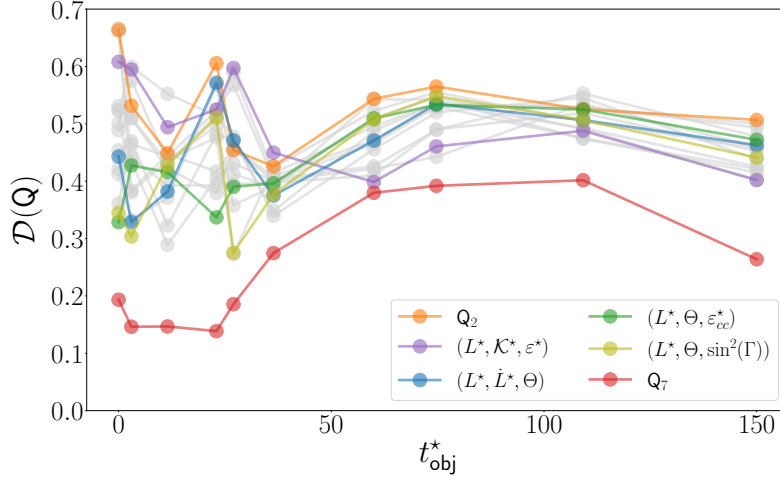


Figure 16: Ability of the various state vectors \mathbf{Q} to infer the initial conditions from the measure $\mathcal{D}(\mathbf{Q})$ evaluated along the inertial DNS trajectory introduced in the figure 5.

use of all the 0D quantities, \mathbf{Q}_8 , allows to well recover the initial conditions. The loss of memory of the initial conditions appears progressively, reaching an asymptotic plateau in the self-similar regime. When less information is present, the inference deteriorates and leads to higher values of $\mathcal{D}(\mathbf{Q})$. Still, the measure allows to optimize the state variables for a model. Using $\mathbf{Q}_3 = (L^*, \Theta, \varepsilon_{cc}^*)^T$ for instance is a good trade-off between inference and number of 0D variables.

5. The maximum a posteriori (MAP) model

In this section, we propose a complete modelling approach for the Rayleigh-Taylor instability. The model's state variables consist of 0D quantities selected based on their ability to infer the initial conditions. Therefore, the goal is to forward-propagate this state vector, from \mathbf{Q}^n to \mathbf{Q}^{n+1} , corresponding to a Δt^* time interval later.

We start by applying the Bayesian inference detailed in the previous section 4.1, to derive the posterior distribution $p(t^*, \mathbf{l} | \mathbf{Q}^n)$. Then, we determine the maximum a posteriori (MAP) of this distribution $(t_{\text{map}}^{*n}, \mathbf{l}_{\text{map}}^n) = \text{argmax}(p(t^*, \mathbf{l} | \mathbf{Q}^n))$ and use the neural network surrogate model to propagate forward the state vector. This leads to

$$\mathbf{Q}^n = \hat{\mathbf{Q}}(t_{\text{map}}^{*n}; \mathbf{l}_{\text{map}}^n) \rightarrow \mathbf{Q}^{n+1} = \hat{\mathbf{Q}}(t_{\text{map}}^{*n} + \Delta t^*; \mathbf{l}_{\text{map}}^n) \quad (5.1)$$

The procedure, Eq. (5.1), can be repeated in order to derive the complete evolution of the state vector. This maximum a posteriori (MAP) model propagates the state variables along the most probable trajectory passing through \mathbf{Q}^n . In that respect, it is the best model which can be achieved for a given choice of \mathbf{Q} .

One of the difficulty of the MAP model is to compute $(t_{\text{map}}^{*n}, \mathbf{l}_{\text{map}}^n)$ from \mathbf{Q}^n , which is computationally intensive. Here, to illustrate the procedure and to have access to the uncertainties at every inference, we chose to infer the whole posterior distribution and to take the MAP out of it. However, a more efficient evaluation of the MAP would be to perform a maximum likelihood estimation. It is an optimization procedure that only seeks the maximum of the distribution, avoiding the costly sampling.

In the figures 17 and 18, we present the results derived with various MAP models starting from $t^* = 0$. While it is not surprising that the \mathbf{Q}_7 model (all the 0D variables

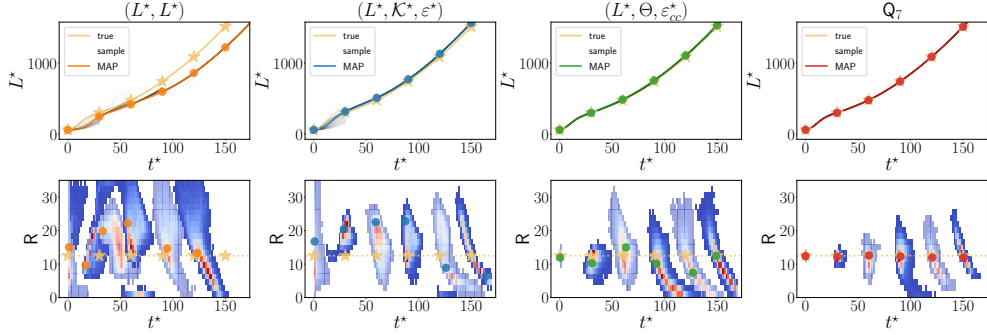


Figure 17: Results of MAP models constructed from Eq. (5.1) with $\Delta t^* = 30$ and using various state vectors indicated in the columns. The first row compares the MAP model to the true trajectory, which corresponds to the inertial trajectory in the figure 5. The second row shows the inferred samples of Reynolds R and time t^* at different instants of the MAP procedure.

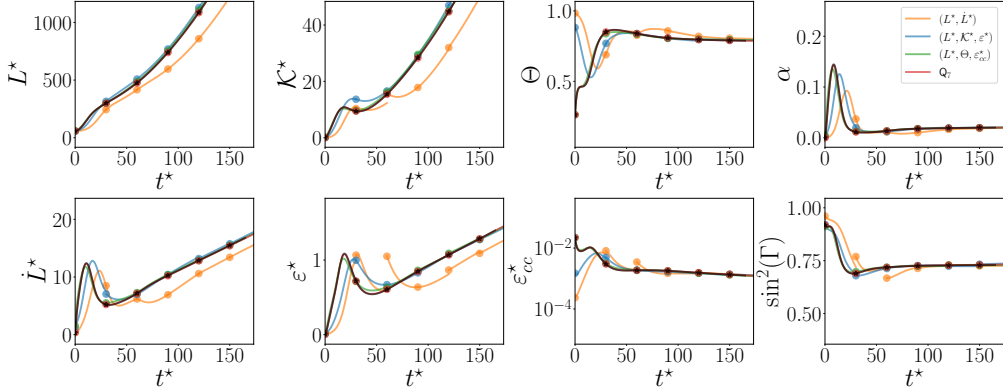


Figure 18: Ability of the various MAP models derived from Eq. (5.1) with $\Delta t^* = 30$ to reconstruct the 0D trajectories corresponding to the inertial case detailed in the figure 5 (black plain line).

without the vertical flux \mathcal{F}^*) is able to reproduce nearly perfectly the target inertial trajectory, less informed MAP model can also perform very well such as $(L^*, \Theta, \varepsilon_{cc}^*)$. Indeed, it is not necessary to infer the initial conditions during the phases with weak dependence on the initial parameters. In the late time self-similar regime for instance, all the trajectories have the same growth rate so the prediction is not too difficult even with a low dimension state vector.

Notably, the trajectories obtained from the MAP model are almost continuous in their state variables (following the variance σ of the likelihood), but not necessarily differentiable as the inferred MAP initial conditions can jump from one extrema to another. This is particularly true for Q_2 which exhibits multi-modal posterior distributions. This explains the deviation of the MAP Q_2 model from the DNS trajectory.

6. Conclusion

This work explores the memory of Rayleigh-Taylor turbulence, focusing specifically on how the mixing layer retains knowledge of its initial conditions. From a large dataset of approximately 500 highly resolved DNS, performed at low Atwood number using the *Stratospec* code, we derive a surrogate model based on a physics-informed neural network strategy. The soft and hard physical constraints imposed on the neural network enable the high-fidelity and cost-effective reproduction of the time evolution of 0D turbulent quantities, at given inputs such as the time and the four non dimensional numbers parametrizing the initial interface. We then employ this surrogate model to conduct a sensitivity analysis across a broad initial domain, covering both inertial and diffusive trajectories, in order to untangle the effects of the initial conditions. It is demonstrated that, although the self-similar growth parameter is nearly constant at $\alpha \approx 0.020$ in the late time regime, consistently with a mode coupling phenomenology, the virtual time origin t_∞^* varies sensitively with the initial Reynolds number, interface steepness, bandwidth and to a lesser degree diffusion thickness. This variability explains why the mixing zone variance continues to grow, being substantially fed during the initial stages of the Rayleigh-Taylor dynamics and peaking around the transition to turbulence. Knowledge of the initial mixing zone width reduces uncertainties but cannot eliminate them entirely. This aspect can be attributed to the significant roles of the molecular mixing and the anisotropy of RT turbulence, which are not fully captured by measurements of mixing size alone. Conversely, whether the initial perturbations have a large or small band width triggers a mode coupling or mode competition phenomenology. This also plays a role in the dynamics particularly around the cut-off wavenumber. In such cases, a large band increases the likelihood of having at least one unstable mode, leading to a distinctly different dynamics.

In order to identify key quantities that conserve the memory of Rayleigh-Taylor turbulence, we perform a classical Bayesian inference to recover the initial conditions and the measurement time from a set of 0D turbulent variables. We employ a MCMC parallel tempering algorithm to compute the posterior distributions, which, in some cases, can be multi-modal, accommodating both inertial and diffusive trajectories. The quality of the reconstruction is monitored throughout the different phases of the RT instability, revealing a rapid expansion of the posterior at the transition to turbulence. As expected, incorporating more 0D variables into the observation set improves the inference quality. By quantifying the discrepancy between the inferred and the true parameters of a trajectory, we identify which sets of 0D quantities best conserve the memory of RT turbulence. These sets provide promising candidates for modelling.

Finally, we introduce the maximum a posteriori (MAP) model. By identifying the peak of the posterior distribution and advancing the state variables forward with the surrogate model –parametrized by the inferred initial conditions– we achieve precise predictions of the RT dynamics from the initial stages through the late time self-similar regime. As this model adheres to the trajectories of the surrogate model, it inherits all its beneficial properties stemming from the physics-informed approach. Thus, this model represents the optimal solution achievable with the state vector \mathbf{Q} , adhering to the most probable trajectories indicated by the MAP estimate. Furthermore, having complete knowledge of the posterior distribution allows to quantify the uncertainties associated with these predictions (Xiao & Cinnella 2019). This methodology, applied here to the RT problem, is adaptable to other types of flows and marks a significant step toward improved predictions of turbulent mixing layers.

The simulations were performed at the french TGCC center.

Appendix A. Physics-informed neural network as a surrogate model for the RT database

In order to emulate DNS dynamics, we consider a multi-layer perceptron (MLP), which is classically used for building deep neural network architectures. It takes as inputs the initial conditions \mathbf{l} and the time t^* , and returns the associated prediction of the dynamical quantities $\mathbf{Q}_8(t^*; \mathbf{l}) = (L^*, \dot{L}^*, \mathcal{K}^*, \varepsilon^*, \Theta, \varepsilon_{cc}^*, \mathcal{F}^*, \sin^2(\Gamma))^T$. The time derivative \dot{L}^* is directly computed by auto-differentiation of L^* with respect to t^* . The MLP consists of 7 hidden layers, each containing 32 neurons, with Softplus activation functions, totaling 6792 parameters. The architecture has been meticulously designed to ensure physical consistency. We are particularly interested in performing (reasonable) time extrapolations. A simple approach is to square the output of the last neuron, corresponding to L^* , to capture its quadratic time growth at later stages. This is because a fully activated Softplus MLP will produce a linear response to its inputs, which include time. This approach is referred to as 'hard constraints' in the literature, as these properties are enforced by the architecture, and is represented by the neuron T in the figure 6.

The MLP parameters are optimized during the training stage in order to minimize the loss function \mathcal{J}_{tot} which is composed of two parts:

$$\mathcal{J}_{\text{tot}} = \mathcal{J}_{\text{Data}} + \mathcal{J}_{\text{PI}}, \text{ with} \quad (\text{A } 1a)$$

$$\mathcal{J}_{\text{Data}} = \sum_{t_n^*, \mathbf{l}_m \in \mathcal{D}_{\text{DNS}}} \beta_{nm}^{\text{Data}} \left\| \text{norm}_{01} \left(\mathbf{Q}_8(t_n^*; \mathbf{l}_m) - \widehat{\mathbf{Q}}_8(t_n^*; \mathbf{l}_m) \right) \right\|^2, \text{ and} \quad (\text{A } 1b)$$

$$\mathcal{J}_{\text{PI}} = \sum_{u \in \mathcal{U}} \sum_{t_n^*, \mathbf{l}_m \in \mathcal{D}_{\text{coll}}} \beta_{nm}^{\text{PI}} \|\mathcal{J}_u(t_n^*; \mathbf{l}_m)\|^2. \quad (\text{A } 1c)$$

The supervised part $\mathcal{J}_{\text{Data}}$, Eq. (A 1b), measures the discrepancy between the normalized surrogate predictions and their DNS counterpart. It is evaluated on a time and initial condition sampled domain \mathcal{D}_{DNS} . The diagonal matrix \mathbf{N} normalizes the 0D quantities in a $[0, 1]$ interval to facilitate training. The weight coefficients β_{nm}^{Data} equal one except at $t_n^* = 0$ where it takes higher values to enforce the right initial conditions.

The unsupervised (physics-informed) part \mathcal{J}_{PI} , Eq. (A 1c), penalizes predictions which do not satisfy a list \mathcal{U} of physical constraints u and evaluated on a set of sampled collocation times and initial conditions $\mathcal{D}_{\text{coll}}$. Therefore \mathcal{J}_u corresponds to the remaining of equations corresponding to the physical constraints such as: The kinetic energy and concentration variance conservations (2.9a)-(2.9b), the self-similar relation (2.10), the positivity of \dot{L} and the dimensional relation $0 = L_0^* - 3/2R\partial L_0^*/\partial R$ expressing the fact that the initial mixing zone width does not depend on the acceleration (or R). The weight coefficients, β_{nm}^{PI} , allow to balance the constraints with each other and to use different sets of collocation points for the constraints. These physics-informed terms are referred to as soft constraints, as the properties are encouraged rather than enforced. To get the most out of it, it is evaluated both at the DNS data points and at randomly drawn collocation points in an extended domain, in order to guide the training towards plausible solutions, even in extrapolation. In practice, several combinations of the weight coefficients are tried and in the end the best performing surrogate is chosen.

The surrogate model is implemented with the PyTorch deep-learning framework (Paszke *et al.* 2019). The MLP parameters are initialized with the Xavier normal procedure and are optimized using the Adam algorithm (Kingma & Ba 2014) with a learning rate of 5×10^{-4} on a NVIDIA A100 GPU, for 2×10^4 epochs done in approximately 80 minutes.

A training dataset containing 294 trajectories (of 300 time points each) is used for optimization and a validation dataset containing 126 is used to monitor overfitting, while the remaining 47 are kept for a posteriori test. At every epoch, the complete loss is evaluated using batches of 25% the size of the training dataset. In addition, the unsupervised part is also evaluated at random points 5% the size of the training dataset.

Appendix B. Computing the Sobol indices

In the Rayleigh-Taylor configuration, knowing the initial conditions \mathbf{l} and the time t^* allows for the complete determination of a zero-dimensional dynamics $q(t^*; \mathbf{l})$. However, if these input parameters are unknown, the dynamics may vary substantially. Sensitivity analysis (SA) describes how uncertainty in the inputs influences this variance and, therefore, identifies the parameters (or group of parameters) that contribute most significantly to it.

A simple SA can be conducted by varying one input at a time while keeping the others constant. This approach is referred to as a local SA. It has the advantage of being straightforward to perform and incurs a very low computational cost. However, it does not account for interaction effects and its effectiveness depends on the point around which the local SA is conducted (Saltelli *et al.* 2019). On the other hand, a global SA overcomes these limitations but requires a significantly higher computational cost, which is mitigated by using a surrogate model.

In this paper, we employed a variance-based global SA, see Saltelli *et al.* (2008) for a comprehensive overview. It consists in decomposing the output in a sum of increasing dimension orthogonal functions such that

$$q(\mathbf{l}) = E[q] + \sum_{i \in \mathbf{l}} q_i(i) + \sum_{i \in \mathbf{l}} \sum_{j \in \mathbf{l}, j \neq i} q_{ij}(i, j) + \dots + q_{\text{RBSD}}(\mathbf{l}). \quad (\text{B } 1)$$

Here we omit the time t^* dependence for simplification. The functions up to second-order are thus defined as

$$q_i(i) = E[q|i] - E[q] \quad q_{ij}(i, j) = E[q|i, j] - q_i(i) - q_j(j) - E[q] \quad (\text{B } 2)$$

This leads to the Hoeffding-Sobol decomposition of the variance,

$$\begin{aligned} V[q] &= \sum_{i \in \mathbf{l}} V[q_i(i)] + \sum_{i \in \mathbf{l}} \sum_{j \in \mathbf{l}, j \neq i} V[q_{ij}(i, j)] + \dots + V[q_{\text{RBSD}}(\mathbf{l})] \\ &= \sum_{i \in \mathbf{l}} V[q_i(i)] + \text{interactions} \end{aligned} \quad (\text{B } 3)$$

where $V[q_i(i)] = V[E[q|i]]$ is known as the first-order partial variance. It represents the part of the variance that is due to a single input parameter $i \in \mathbf{l}$. It expresses the effect of i . By dividing this partial variance by the total variance $V[q]$, one obtains the so-called first order Sobol index. Its explicit formulation involves several integrals that are analytically intractable and in relatively high dimension, so in order to perform SA one must use efficient approximating techniques. In this work we used an efficient Monte Carlo based procedure first introduced by Sobol (1993). It relies on the observation that $V[E[q|i]]$ equals the covariance $\text{Cov}[q, q']$, where q and q' are computed from two sets of inputs that share the same value for input i only. Therefore, if we construct two independent and identically distributed samples q_n and q'_n of size N , leading to the following estimate

(Saltelli *et al.* 2010)

$$V[E[q|i]] \simeq \frac{1}{N} \sum_{n=1}^N q_n q'_n - \left(\frac{1}{N} \sum_{n=1}^N q_n \right)^2 \quad (\text{B 4})$$

where it is assumed that $\left(\frac{1}{N} \sum_{n=1}^N q_n \right)^2 = \left(\frac{1}{N} \sum_{n=1}^N q'_n \right)^2$. In our study, we used $N = 3 \times 10^4$ samples, where the inputs were randomly drawn within a hypercubic domain because the variance-based global SA requires that the inputs not be correlated. This procedure was executed for various time steps t^* to reconstruct the time evolution of the initial conditions' main effects. Additionally, this procedure was repeated 20 times, and the results were averaged to obtain a robust estimation through bootstrapping. This was particularly important for assessing the second-order interaction effects, although we ultimately decided to exclude these from the paper due to their minimal contribution.

Appendix C. Bayesian inference by MCMC

As introduced in Section 4.1, directly evaluating the joint posterior from Bayes' rule is computationally heavy due to the evaluation of the marginal law $p(\mathbf{Q})$. Markov Chain Monte Carlo (MCMC) is a general class of sampling algorithms that overcomes this issue by avoiding the need to compute this term. It involves constructing a Markov chain whose stationary distribution is the target distribution we seek, in our case, the joint posterior. This means that, after a convergence stage, all samples generated by the Markov chain will follow the target distribution. See Gelman *et al.* (2021) for a comprehensive introduction.

In this work, as we expect our joint posterior to be multimodal in some cases, we utilized the parallel tempering algorithm with a Metropolis-Hastings random walk (Metropolis *et al.* 1953; Hastings 1970; Geyer 1991; Falcioni & Deem 1999; Sambridge 2014). This algorithm relies on two key elements. First, an artificial dimension known as the temperature T is added to the problem, necessitating that we now sample the distribution

$$p(\mathbf{l}, t^*, T | \mathbf{Q}) = p(\mathbf{l}, t^* | \mathbf{Q})^{1/T}. \quad (\text{C 1})$$

This temperature has discrete values and one can remark that for $T = 1$, we recover our target distribution. In addition, for $T > 1$, the distribution $p(\mathbf{l}, t^*, T | \mathbf{Q})$ becomes a flattened version of $p(\mathbf{l}, t^* | \mathbf{Q})$. The second key idea is to run several Markov chains in parallel, that have different temperatures $T \geq 1$. These chains independently advance following a random walk and every once in a while temperature swaps between those chains are proposed and either accepted or rejected according to an acceptance rule very similar to Metropolis-Hastings'. This allows an efficient exploration of the whole space, no matter how sharp and multi-modal the original joint posterior is. Indeed, a classical Metropolis-Hastings algorithm would get stuck in a high-probability region and would have trouble exploring another if the two peaks are separated by a low-probability region. In parallel tempering, a chain with $T = 1$ would get stuck but a higher-temperature chain would not. So the latter could reach the second peak and then swap temperature with the former, allowing an efficient sampling of our joint posterior (by collecting samples drawn at $T = 1$).

For each inference, we use $M = 10$ parallel chains with temperatures logarithmically ranging between 1 and 10^4 . We perform $N = 5 \times 10^5$ iterations and discard the first 10^5 iterations that correspond to the convergence stage. At every iteration, we either propose a temperature swap between pairs of chains, with probability $p_{\text{swap}} = 0.25$, or

make a random walk step for every parallel chain, with probability $1 - p_{\text{swap}} = 0.75$. The random walk involves making a random step starting from the last state (l_n, t_n^*) of the chain. We define the proposal distribution $\mathcal{P}(l_j, t_j^* | l_n, t_n^*)$ as a Gaussian with mean (l_n, t_n^*) and covariance matrix \mathbf{C} chosen diagonal with standard deviations set to be equal to 1% of the overall domain range. In practice, we conduct two independent parallel tempering runs to assess the statistical convergence of the results, as suggested in Roy (2020); Vehtari *et al.* (2021).

REFERENCES

- ABU-SHAWAREB, H, ACREE, R, ADAMS, P, ADAMS, J, ADDIS, B, ADEN, R, ADRIAN, P, AFEYAN, BB, AGGLETON, M, AGHAIAN, L *et al.* 2024 Achievement of target gain larger than unity in an inertial fusion experiment. *Physical Review Letters* **132** (6), 065102.
- ANDREWS, M. J. & SPALDING, D. B. 1990 A simple experiment to investigate two-dimensional mixing by Rayleigh–Taylor instability. *Physics of Fluids A: Fluid Dynamics* **2** (6), 922–927.
- ASLANGIL, DENIS, LAWRIE, ANDREW GW & BANERJEE, ARINDAM 2022 Effects of variable deceleration periods on Rayleigh–Taylor instability with acceleration reversals. *Physical Review E* **105** (6), 065103.
- BANERJEE, ARINDAM, GORE, ROBERT A. & ANDREWS, MALCOLM J. 2010 Development and validation of a turbulent-mix model for variable-density and compressible flows. *Phys. Rev. E* **82**, 046309.
- BIAN, XIN, ALUIE, HUSSEIN, ZHAO, DONGXIAO, ZHANG, HUASEN & LIVESCU, DANIEL 2020 Revisiting the late-time growth of single-mode Rayleigh–Taylor instability and the role of vorticity. *Physica D: Nonlinear Phenomena* **403**, 132250.
- BOFFETTA, G. & MAZZINO, A. 2017 Incompressible Rayleigh–Taylor turbulence. *Annual Review of Fluid Mechanics* **49** (1), 119–143.
- BOFFETTA, G., MAZZINO, A. & MUSACCHIO, S. 2011 Effects of polymer additives on Rayleigh–Taylor turbulence. *Phys. Rev. E* **83**, 056318.
- BRIARD, ANTOINE, GOSTIAUX, LOUIS & GRÉA, BENOÎT-JOSEPH 2020 The turbulent faraday instability in miscible fluids. *Journal of Fluid Mechanics* **883**, A57.
- BRIARD, ANTOINE, GRÉA, BENOÎT-JOSEPH & NGUYEN, FLORIAN 2022 Growth rate of the turbulent magnetic Rayleigh–Taylor instability. *Phys. Rev. E* **106**, 065201.
- BRUNTON, S. L., NOACK, B. R. & KOUMOUTSAKOS, P. 2019 Machine learning for fluid mechanics. *Annual Review of Fluid Mechanics* .
- BUARIA, DHAWAL & SREENIVASAN, KATEPALLI R. 2023 Forecasting small-scale dynamics of fluid turbulence using deep neural networks. *Proceedings of the National Academy of Sciences* **120** (30), e2305765120, publisher: Proceedings of the National Academy of Sciences.
- CAVELIER, M, GRÉA, B-J, BRIARD, A & GOSTIAUX, L 2022 The subcritical transition to turbulence of faraday waves in miscible fluids. *Journal of Fluid Mechanics* **934**, A34.
- CHANDRASEKHAR, S. 1961 *Hydrodynamic and Hydromagnetic Stability*. Dover Publ.
- COOK, A. & CABOT, W. 2006 Reynolds number effects on Rayleigh–Taylor instability with possible implications for type-ia supernovae. *Nat. Phys.* **2**, 562–568.
- COOK, ANDREW W, CABOT, WILLIAM & MILLER, PAUL L 2004 The mixing transition in Rayleigh–Taylor instability. *Journal of Fluid Mechanics* **511**, 333–362.
- COOK, A. W. & DIMOTAKIS, P. E. 2001 Transition stages of Rayleigh–Taylor instability between miscible fluids. *J. Fluid Mech.* **443**, 69–99.
- DALZIEL, SB, LINDEN, PF & YOUNGS, DL 1999 Self-similarity and internal structure of turbulence induced by Rayleigh–Taylor instability. *Journal of fluid Mechanics* **399**, 1–48.
- DAVIES WYKES, M. S. & DALZIEL, S. B. 2014 Efficient mixing in stratified flows: Experimental study of a Rayleigh–Taylor unstable interface within an otherwise stable stratification. *Journal of Fluid Mechanics* **756**, 1027.
- DIMONTE, GUY 2004 Dependence of turbulent Rayleigh–Taylor instability on initial perturbations. *Physical Review E* **69** (5), 056305.
- DIMONTE, GUY, RAMAPRABHU, PRAVEEN & ANDREWS, MALCOLM 2007 Rayleigh–Taylor instability with complex acceleration history. *Physical Review E* **76** (4), 046313.
- DIMONTE, G., YOUNGS, D. L., DIMITS, A., WEBER, S., MARINAK, M., WUNSCH, S., GARASI,

- C., ROBINSON, A., ANDREWS, M. J., RAMAPRABHU, P., CALDER, A. C., FRYXELL, B., BIELLO, J., DURSI, L., MACNEICE, P., OLSON, K., RICKER, P., ROSNER, R., TIMMES, F., TUFO, H., YOUNG, Y.-N. & ZINGALE, M. 2004 A comparative study of the turbulent Rayleigh–Taylor instability using high-resolution three-dimensional numerical simulations: The Alpha-Group collaboration. *Phys. Fluids* **16** (5), 1668–1693.
- DUFF, RE, HARLOW, FH & HIRT, CW 1962 Effects of diffusion on interface instability between gases. *The Physics of Fluids* **5** (4), 417–425.
- DURASAMY, KARTHIK, IACCARINO, GIANLUCA & XIAO, HENG 2019 Turbulence Modeling in the Age of Data. *Annual Review of Fluid Mechanics* **51** (1), 357–377, eprint: <https://doi.org/10.1146/annurev-fluid-010518-040547>.
- FALCIONI, M. & DEEM, M. W. 1999 A biased monte carlo scheme for zeolite structure solution. *J. Chem. Phys.* .
- FERMI, E & VON NEWMAN, J 1951 Taylor instability of an incompressible liquid 26 e fermi 1962 collected papers.
- FERNANDO, HARINDRA JS 1991 Turbulent mixing in stratified fluids. *Annual review of fluid mechanics* **23** (1), 455–493.
- GELMAN, A., CARLIN, J. B., STERN, H. S., DUNSON, D. B., VEHTARI, A. & RUBIN, D. B. 2021 Bayesian data analysis .
- GEYER, C. J. 1991 Markov chain monte carlo maximum likelihood. *Computing Science and Statistics: Proceedings of the 23rd Symposium on the Interface* .
- GONCHAROV, V. N. 2002 Analytical model of nonlinear, single-mode, classical Rayleigh–Taylor instability at arbitrary atwood numbers. *Phys. Rev. Letters* **88** (13), 134502–4.
- GRÉA, B.-J. 2013 The rapid acceleration model and the growth rate of a turbulent mixing zone induced by Rayleigh–Taylor instability. *Phys. Fluids* **25** (1), 015118 (20 pages).
- GRÉA, B.-J. & BRIARD, A. 2019 Frozen waves in turbulent mixing layers. *Phys. Rev. Fluids* **4**, 064608.
- GRÉA, BENOÎT-JOSEPH & BRIARD, ANTOINE 2023 Inferring the magnetic field from the Rayleigh–Taylor instability. *The Astrophysical Journal* **958** (2), 164.
- GREGG, MICHAEL C, D’ASARO, ERIC A, RILEY, JAMES J & KUNZE, ERIC 2018 Mixing efficiency in the ocean. *Annual review of marine science* **10**, 443–473.
- GUASTONI, LUCA, GÜEMES, ALEJANDRO, IANIRO, ANDREA, DISCETTI, STEFANO, SCHLATTER, PHILIPP, AZIZPOUR, HOSSEIN & VINUESA, RICARDO 2021 Convolutional-network models to predict wall-bounded turbulence from wall quantities. *Journal of Fluid Mechanics* **928**, A27.
- HASTINGS, W. K. 1970 Monte carlo sampling methods using markov chains and their applications. *Biometrika* .
- HILLIER, ANDREW 2018 The magnetic Rayleigh–Taylor instability in solar prominences. *Rev. Mod. Plasma Phys.* **2** (1).
- HURRICANE, OA, CALLAHAN, DA, CASEY, DT, CHRISTOPHERSON, AR, KRITCHER, AL, LANDEN, OL, MACLAREN, SA, NORA, R, PATEL, PK, RALPH, J *et al.* 2024 Energy principles of scientific breakeven in an inertial fusion experiment. *Physical Review Letters* **132** (6), 065103.
- KARNIADAKIS, GEORGE EM, KEVREKIDIS, IOANNIS G, LU, LU, PERDIKARIS, PARIS, WANG, SIFAN & YANG, LIU 2021 Physics-informed machine learning. *Nature Reviews Physics* **3** (6), 422–440.
- KINGMA, D. & BA, J. 2014 Adam: A method for stochastic optimization. *International Conference on Learning Representations* .
- KORD, ALI & CAPECELATRO, JESSE 2019 Optimal perturbations for controlling the growth of a Rayleigh–Taylor instability. *Journal of Fluid Mechanics* **876**, 150–185.
- LAYZER, DAVID 1955 On the instability of superposed fluids in a gravitational field. *apj* **122**, 1.
- LINDL, JOHN 1995 Development of the indirect-drive approach to inertial confinement fusion and the target physics basis for ignition and gain. *Physics of plasmas* **2** (11), 3933–4024.
- LING, J., KURZAWSKI, A. & TEMPLETON, J. 2016 Reynolds averaged turbulence modelling using deep neural networks with embedded invariance. *Journal of Fluid Mechanics* .
- LIVESCU, D 2013 Numerical simulations of two-fluid turbulent mixing at large density ratios and applications to the Rayleigh–Taylor instability. *Philosophical Transactions of the Royal Society A: Mathematical, Physical and Engineering Sciences* **371** (2003), 20120185.

- LIVESCU, D, WEI, T & BRADY, PT 2021 Rayleigh–Taylor instability with gravity reversal. *Physica D: nonlinear phenomena* **417**, 132832.
- METROPOLIS, N., ROSENBLUTH, A. W., ROSENBLUTH, M. N. & TELLER, A. H. TELLER, E. 1953 Equation of state calculations by fast computing machines. *J. Chem. Phys.* .
- MORGAN, BRANDON E 2022 Large-eddy simulation and Reynolds-averaged Navier–Stokes modeling of three Rayleigh–Taylor mixing configurations with gravity reversal. *Physical Review E* **106** (2), 025101.
- MORGAN, BRANDON E & BLACK, WOLFGANG J 2020 Parametric investigation of the transition to turbulence in Rayleigh–Taylor mixing. *Physica D: Nonlinear Phenomena* **402**, 132223.
- MORGAN, B. E., OLSON, B. J., WHITE, J. E. & MCFARLAND, J. A. 2017 Self-similarity of a Rayleigh–Taylor mixing layer at low atwood number with a multimode initial perturbation. *Journal of Turbulence* **18** (10), 973–999.
- MORGAN, BRANDON E & WICKETT, MICHAEL E 2015 Three-equation model for the self-similar growth of Rayleigh–Taylor and richtmyer-meskov instabilities. *Physical Review E* **91** (4), 043002.
- MUESCHKE, NICHOLAS J, ANDREWS, MALCOLM J & SCHILLING, OLEG 2006 Experimental characterization of initial conditions and spatio-temporal evolution of a small-Atwood-number Rayleigh–Taylor mixing layer. *Journal of Fluid Mechanics* **567**, 27–63.
- NAKAI, S & TAKABE, H 1996 Principles of inertial confinement fusion-physics of implosion and the concept of inertial fusion energy. *Reports on progress in physics* **59** (9), 1071.
- OLIVIER GRÉGOIRE, DENIS SOUFLAND & GAUTHIER, SERGE 2005 A second-order turbulence model for gaseous mixtures induced by richtmyer—meshkov instability. *Journal of Turbulence* **6**, N29.
- PASZKE, ADAM, GROSS, SAM, MASSA, FRANCISCO, LERER, ADAM, BRADHURY, JAMES, CHANAN, GREGORY, KILLEEN, TREVOR, LIN, ZEMING, GIMELSEIN, NATALIA, ANTIGA, LUCA, DESMAISON, ALBAN, KOPF, ANDREAS, YANG, EDWARD, DEVITO, ZACHARY, RAISON, MARTIN, TEJANI, ALYKHAN, CHILAMKURTHY, SASANK, STEINER, BENOIT, FANG, LU, BAI, JUNJIE & CHINTALA, SOUMITH 2019 An imperative style, high-performance deep learning library. *arXiv:191201703* .
- PORTH, OLIVER, KOMISSAROV, SERGUEI S. & KEPPENS, RONY 2014 Rayleigh–Taylor instability in magnetohydrodynamic simulations of the Crab nebula. *Monthly Notices of the Royal Astronomical Society* **443** (1), 547–558.
- POUJADE, OLIVIER & PEYBERNES, MATHIEU 2010 Growth rate of Rayleigh–Taylor turbulent mixing layers with the foliation approach. *Physical Review E* **81** (1), 016316.
- RAMAPRABHU, P & ANDREWS, MJ 2004 Experimental investigation of Rayleigh–Taylor mixing at small atwood numbers. *Journal of Fluid Mechanics* **502**, 233–271.
- RAMAPRABHU, P, DIMONTE, GUY & ANDREWS, MJ 2005 A numerical study of the influence of initial perturbations on the turbulent Rayleigh–Taylor instability. *Journal of Fluid Mechanics* **536**, 285–319.
- RAMAPRABHU, P., DIMONTE, G., YOUNG, Y. N., CALDER, A. C. & FRYXELL, B. 2006 Limits of the potential flow approach to the single-mode Rayleigh–Taylor problem. *Phys. Rev. E* **74**, 06308.
- RAMAPRABHU, PRAVEEN, KARKHANIS, VARAD & LAWRIE, ANDREW GW 2013 The Rayleigh–Taylor instability driven by an accel-decel-accel profile. *Physics of Fluids* **25** (11).
- RAMSHAW, JOHN D 1998 Simple model for linear and nonlinear mixing at unstable fluid interfaces with variable acceleration. *Physical review E* **58** (5), 5834.
- RAYLEIGH 1882 Investigation of the Character of the Equilibrium of an Incompressible Heavy Fluid of Variable Density*. *Proceedings of the London Mathematical Society* **s1-14** (1), 170–177.
- RISTORCELLI, J. R. & CLARK, T. T. 2004 Rayleigh–Taylor turbulence: self-similar analysis and direct numerical simulations. *Journal of Fluid Mechanics* **507**, 213–253.
- ROBERTS, MS & JACOBS, JW 2016 The effects of forced small-wavelength, finite-bandwidth initial perturbations and miscibility on the turbulent Rayleigh–Taylor instability. *Journal of Fluid Mechanics* **787**, 50–83.
- ROY, V. 2020 Convergence diagnostics for markov chain monte carlo. *Annual Review of Statistics and Its Application* .
- SALTELLI, ANDREA, ALEKSANKINA, KSENIA, BECKER, WILLIAM, FENNELL, PAMELA, FER-

- RETTI, FEDERICO, HOLST, NIELS, LI, SUSHAN & WU, QIONGLI 2019 Why so many published sensitivity analyses are false: A systematic review of sensitivity analysis practices. *Environmental modelling & software* .
- SALTELLI, ANDREA, ANNONI, PAOLA, AZZINI, IVANO, CAMPOLONGO, FRANCESCA, RATTO, MARCO & TARANTOLA, STEFANO 2010 Variance based sensitivity analysis of model output. design and estimator for the total sensitivity index. *Computer Physics Communications* .
- SALTELLI, ANDREA, RATTO, MARCO, ANDRES, TERRY, CAMPOLONGO, FRANCESCA, CARIBONI, JESSICA, GATELLI, DEBORA, SAISANA, MICHAELA & TARANTOLA, STEFANO 2008 Global sensitivity analysis. *The Primer* .
- SAMBRIDGE, M. 2014 A parallel tempering algorithm for probabilistic sampling and multimodal optimization. *Geophys. J. Int.* .
- SCHILLING, OLEG & MUESCHKE, NICHOLAS J 2017 Turbulent transport and mixing in transitional rayleigh-taylor unstable flow: A priori assessment of gradient-diffusion and similarity modeling. *Physical Review E* **96** (6), 063111.
- SCHWARZKOPF, JOHN D, LIVESCU, DANIEL, GORE, ROBERT A, RAUENZAHN, RICK M & RISTORCELLI, J RAYMOND 2011 Application of a second-moment closure model to mixing processes involving multicomponent miscible fluids. *Journal of Turbulence* (12), N49.
- SHARP, D.H. 1984 An overview of Rayleigh-Taylor instability. *Physica D: Nonlinear Phenomena* **12** (1), 3 – 18.
- SOBOL, I. M. 1993 Sensitivity estimates for nonlinear mathematical models. *Mathematical Modelling and Computational Experiments 1* .
- SOLERA-RICO, ALBERTO, SANMIGUEL VILA, CARLOS, GÓMEZ-LÓPEZ, MIGUEL, WANG, YUNING, ALMASHJARY, ABDULRAHMAN, DAWSON, SCOTT T. M. & VINUESA, RICARDO 2024 beta-Variational autoencoders and transformers for reduced-order modelling of fluid flows. *Nature Communications* **15** (1), 1361, publisher: Nature Publishing Group.
- SOULARD, O., GRIFFOND, J. & GRÉA, B.-J. 2015 Large-scale analysis of unconfined self-similar Rayleigh–Taylor turbulence. *Physics of Fluids* **27** (9).
- TAYLOR, GEOFFREY INGRAM 1950 The instability of liquid surfaces when accelerated in a direction perpendicular to their planes. i. *Proceedings of the Royal Society of London. Series A. Mathematical and Physical Sciences* **201** (1065), 192–196.
- THORNBUR, BEN, DRIKAKIS, DIMITRIS, YOUNGS, DL & WILLIAMS, RJR 2010 The influence of initial conditions on turbulent mixing due to richtmyer–meshkov instability. *Journal of Fluid Mechanics* **654**, 99–139.
- VEHTARI, A., GELMAN, A., SIMPSON, D., CARPENTER, B. & BÜRKNER, P.-C. 2021 Rank-normalization, folding, and localization: An improved \hat{R} for assessing convergence of mcmc (with discussion). *Bayesian Analysis* .
- VICICONTE, GIOVANNI, GRÉA, BENOÎT-JOSEPH, GODEFERD, FABIEN S., ARNAULT, PHILIPPE & CLÉROUIN, JEAN 2019 Sudden diffusion of turbulent mixing layers in weakly coupled plasmas under compression. *Phys. Rev. E* **100**, 063205.
- VLADIMIROVA, NATALIA & CHERTKOV, MICHAEL 2009 Self-similarity and universality in Rayleigh–Taylor, Boussinesq turbulence. *Physics of Fluids* **21** (1).
- XIAO, HENG & CINNELLA, PAOLA 2019 Quantification of model uncertainty in rans simulations: A review. *Progress in Aerospace Sciences* **108**, 1–31.
- YOUNG, Y.-N., TUFO, H., DUBEY, A. & ROSNER, R. 2001 On the miscible Rayleigh-Taylor instability: two and three dimensions. *J. Fluid Mech.* **447**, 377–408.
- YOUNGS, D.L. 2013 The density ratio dependence of self-similar Rayleigh–Taylor mixing. *Philosophical Transactions of the Royal Society A: Mathematical* **3** (71).
- ZHOU, YE 2017 Rayleigh–Taylor and Richtmyer–Meshkov instability induced flow, turbulence, and mixing. ii. *Physics Reports* **723–725**, 1–160, rayleigh–Taylor and Richtmyer–Meshkov instability induced flow, turbulence, and mixing. II.
- ZHOU, YE, WILLIAMS, ROBIN J.R., RAMAPRABHU, PRAVEEN, GROOM, MICHAEL, THORNBUR, BEN, HILLIER, ANDREW, MOSTERT, WOUTER, ROLLIN, BERTRAND, BALACHANDAR, S., POWELL, PHILLIP D., MAHALOV, ALEX & ATTAL, N. 2021 Rayleigh–Taylor and Richtmyer–Meshkov instabilities: A journey through scales. *Physica D: Nonlinear Phenomena* **423**, 132838.
- ZHU, LU, JIANG, XIANYANG, LEFAUVE, ADRIEN, KERSWELL, RICH R. & LINDEN, P. F. 2024

New insights into experimental stratified flows obtained through physics-informed neural networks. *Journal of Fluid Mechanics* **981**, R1.